Statistics of weakly nonlinear waves on currents with strong vertical shear

Zibo Zheng[1],[*] Yan Li[1,2,b], and Simen Å. Ellingsen[1‡]

[1]*Department of Energy and Process Engineering,*

Norwegian University of Science and Technology, N-7491 Trondheim, Norway,

[2]*Department of Mathematics, University of Bergen, N-5020 Bergen, Norway.*

(Dated: December 13, 2022)

We investigate how the presence of a vertically sheared current affects wave statistics, including the probability of rogue waves, and apply it to a real-world case using measured spectral and shear current data from the Mouth of the Columbia River. A theory for weakly nonlinear waves valid to second order in wave steepness is derived, and used to analyze statistical properties of surface waves; the theory extends the classic theory by Longuet-Higgins [*J. Fluid Mech.* **12**, 3 (1962)] to allow for an arbitrary depth-dependent background flow, $U(z)$, with U the horizontal velocity along the main direction of wave propagation and z the vertical axis. Numerical statistics are collected from a large number of realisations of random, irregular sea-states following a JONSWAP spectrum, on linear and exponential model currents of varying strengths. A number of statistical quantities are presented and compared to a range of theoretical expressions from the literature; in particular the distribution of wave surface elevation, surface maxima, and crest height; the exceedance probability including the probability of rogue waves; the maximum crest height among N_s waves, and the skewness of the surface elevation distribution. We find that compared to no-shear conditions, opposing vertical shear ($U'(z) > 0$) leads to increased wave height and increased skewness of the nonlinear-wave elevation distribution, while a following shear ($U'(z) < 0$) has opposite effects. With the wave spectrum and velocity profile measured in the Columbia River estuary by Zippel & Thomson [*J. Geophys. Res: Oceans* **122**, 3311 (2017)] our second–order theory predicts that the probability of rogue waves is significantly reduced and enhanced during ebb and flood, respectively, adding support to the notion that shear currents need to be accounted for in wave modelling and prediction.

I. INTRODUCTION

Waves in the ocean are almost invariably affected by interaction with their surroundings, ambient currents in particular. While large-scale ocean currents may be approximately depth-independent, this is often not the case for smaller scale currents such as those driven by wind

[b] Corresponding author: yan.li@uib.no

[*] zibo.zheng@ntnu.no

[‡] simen.a.ellingsen@ntnu.no

shear, or currents in the near-shore environment including river deltas and tidal currents. Of particular interests is the role of these environmental factors on the occurrence probability of extremely large waves [1–3], known also as rogue, giant, or freak waves, defined as waves whose amplitude far exceeds that of their surrounding wave field. To this end, many formation mechanisms of rogue waves have been proposed, including (but not limited to) dispersive focusing of linear waves [1], nonlinear effects such as the modulational instability [4] and quartet resonances [5] as well as refraction by currents [6] and bathymetry [7, 8], nonlinear interaction between surface waves and depth transitions [9, 10]. In this paper, our main attention is paid to the effect of a background depth-varying current on the statistics of weakly non-linear waves, rogue wave events in particular.

In order to obtain a proper statistical description of rogue wave events, a theory for second-order interaction of waves in a random sea has been widely used in both analytical [11–18] and numerical studies [19, 20]. In contrast to linear waves in a random sea for which the wave elevation can be represented as a Gaussian random process [21], second-order nonlinear waves can lead to considerable deviations from Gaussian wave statistics due to the steepened crests and flattened troughs caused by second-order (bound) waves. To describe the altered statistics, analytical models for wave crest and elevation distributions have been proposed for deep-water random waves, see, e.g., [13, 15, 17]. These generally agree well with both laboratory and field measurements for narrowband and broadband wave fields (see, e.g., [17, 20, 22–24]) with moderate steepness. In more nonlinear sea states discrepancies arise from third and higher order nonlinear effects, e.g., the well-known Benjamin-Feir instability [4] and the resonant wave quartets [5]. Hence, a second-order theory such as the one we present herein, is limited to the cases where higher-order corrections are comparatively small.

Many studies have suggested several different ways by which the probability of rogue waves is increased in the presence of currents with horizontal, but not vertical, spatial variation (c.f. [25, 26]). A current whose magnitude and direction varies slowly in space relative to the rapidly varying wave phase has mostly been considered as a (local) Doppler shift on the wave dispersion relation and as a medium of refraction in the conservation of wave action [6, 27]. Due to this, White & Fornberg [6] attribute the enhanced probability of larger wave events in currents to the local refraction by currents. Many varieties of the third-order nonlinear Schrödinger equations have been developed for slowly (horizontally) varying currents, see, e.g., [28–30]. An opposing current has been found to lead to strengthened modulational instability [7, 31] and Shrira & Slunyaev [26] found that trapped waves by a jet current can also lead to an enhanced formation probability of rogue waves while Hjelmervik and Trulsen [30] found that a wave impinging on an opposing jet has increased significant wave height, but decreased kurtosis, and *vice versa*. .

The aforementioned works have focused on a current whose velocity profile does not have significant gradients in the vertical direction. Among the studies of waves in a horizontally uniform and depth varying current, a majority have examined waves propagating along or against currents which vary linearly with depth, which in two dimensions permits the use of a velocity potential [32], considerably simplifying the analytical treatment [29, 33–37]. The assumption of a linearly varying current also results in significant simplification of the continuity and Euler momentum equations in three dimensions, based on which a second-order theory for three-dimensional waves was developed by Akselsen and Ellingsen [38]. A uniform vorticity plays a significant role in both the sideband instability and modulational growth rate for weakly nonlinear unidirectional Stokes waves [34, 39]. A positive vorticity, which corresponds to a following current — i.e. $U(z) > 0$ and $U'(z) < 0$ with $U(z)$ the current oriented along the wave propagation direction, z the vertical coordinate, and a prime denotes the derivative — can remove the modulational instability altogether, demonstrated experimentally by Steer *et al.* [40] and Pizzo *et al.* [41] (the definition of positive/negative shear in ref. [40] is different from ours due to a different choice of the coordinate system). Francius and Kharif [42] have extended [34] to two-dimensional Stokes waves where new quartet and quintet instabilities have been discovered arising from the presence of a uniform vorticity, while Abrashkin and Pelinovsky [43] derived a nonlinear Schrödinger equation for arbitrary, weak vertical shear in a Lagrangian framework, generalized in ref. [41].

Realistic natural currents have non-zero curvature in the depth direction which leads to additional effects on wave properties. A number of works, e.g., [44–48], have demonstrated the importance of the depth-varying curvature of a current profile in the wave action equation. Effects of the curvature are wavenumber- and depth-dependent, leading to considerable deviations of the direction and speed of the propagation of wave energy from the cases where the curvature has been neglected [48]. Experimental studies, e.g. [49–51], have confirmed the importance of curvature in wave modelling. Cummins & Swan [49] carried out an experimental study of irregular waves propagating in an arbitrarily depth varying current and the wave spectra measured showed significant differences from those in a uniform and magnitude-equivalent current. It was concluded by Waseda *et al.* [50] from experiments that the variability of the ambient current affected the third-order resonant interaction of wave quartets more than its mean profile did. In field observations, ocean currents are found to have considerable effect on the significant wave height [52], estimation of Stokes drift and particle trajectories [53], and the dissipation of waves through breaking [54].

The objective of the paper is twofold. Firstly, we present a new framework to allow for the interaction of weakly nonlinear surface gravity waves and a vertically sheared current, generalising the work of Longuet-Higgins [11]. Secondly, we implement the new theory numerically to study how a current profile's shear and curvature affect wave statistics, e.g., wave crest distribution and skewness of the surface elevation of random waves.

We highlight that the new framework presented in this paper does not rely on assumptions of weak vertical shear (such as Stewart and Joy [55], Skop [56], Kirby and Chen [57], Zakharov and Shrira [58]) or weak curvature (or 'near-potentiality', e.g., Shrira [59] and Ellingsen and Li [60]). Although these simplifying assumption may be applicable to most realistic situations in the open ocean, their validity should not be taken for granted, and must be properly ascertained [60]. Indeed the shear of a current can be strong in oceanic and coastal waters. For example, a wind-driven shear current in the top few centimetres can have very strong shear (e.g. [61, 62]) and the surface current typically takes values $\sim 3\%$ of the wind speed [63]. Estuarine tidal flow has been found to be very strongly sheared, for instance the Mouth of the Columbia River which we use as example herein [54, 64]. We therefore choose to use the numerical Direct Integration Method (DIM) proposed by Li and Ellingsen [47] to calculate the linear wave surface and velocity fields, being equally applicable to any horizontally-uniform depth-dependent current profile regardless of its magnitude, shear, and curvature. As detailed in Li and Ellingsen [47], the computational cost of the DIM is comparable to that using analytical approximations which involve integration over the water column [55–57, 60], and unlike the aforementioned approximations, it provides an error estimate at little extra cost. The computer code used to generate the results presented in this paper is included as supplementary material online.

This paper is laid out as follows. A second-order theory based on a perturbation expansion, the Direct Integration Method for linear waves [47], and double Fourier integrals for the second-order bound waves is presented in §II. Using the assumption of narrow-banded waves the shear current-modified wave statistics (e.g., skewness and the exceedance probability of wave crest) are derived in §III. With the numerical implementation of the theory detailed in §IV, weakly nonlinear waves in a random sea are examined in §V, for which the linear wave amplitude and phase used for random wave realisations are assumed to follow a Rayleigh distribution and a uniform distribution, respectively, following Tucker *et al.* [65].

II. THEORETICAL DESCRIPTION AND METHODOLOGY

A. Problem statement

We consider three-dimensional surface gravity waves atop a background flow in deep water. Incompressible and inviscid fluids are assumed and the surface tension has been neglected for simplicity. The background flow propagates in the horizontal plane and varies with depth (i.e. vertically sheared). Its 3-dimensional velocity vector is described by $\mathbf{U}_3^*(z^*) = (\mathbf{U}^*(z^*), 0)$, with $\mathbf{U}^*$ the velocity vector in the horizontal plane, z^* the upward axis, and a vanishing vertical component. Dimensional variables are marked with an asterisk. A Cartesian coordinate system is chosen and the still water surface in the absence of waves and flow is located at $z^* = 0$. The surface elevation due to the background flow in the absence of surface waves is described by $z^* = \eta^*$, which is assumed known and whose spatial and temporal variations are comparably negligible to the wave perturbed fields. Neglecting the influence of surface waves on the background flow field, the system of surface waves in a background flow can be described by the continuity and Euler momentum equations as follows (see, e.g., [27])

$$\nabla_3^* \cdot \mathbf{V}_3^* = \ 0, \tag{1}$$

$$\partial_{t^*}\mathbf{V}_3^* + (\mathbf{V}_3^* \cdot \nabla_3^*)\mathbf{U}_3^* + (\mathbf{U}_3^* \cdot \nabla_3^*)\mathbf{V}_3^* + \nabla_3^*\left(P^*/\rho + gz^*\right) = \ -\left(\mathbf{V}_3^* \cdot \nabla_3^*\right)\mathbf{V}_3^*, \tag{2}$$

for $-\infty < z^* < \zeta^* + \eta^*$. Here $\nabla_3^* = (\nabla^*, \partial_{z^*})$ denotes the gradient operator in three dimensions and $\nabla^* = (\partial_{x^*}, \partial_{y^*})$ the gradient in the horizontal plane; $\mathbf{V}_3^* = (\mathbf{u}^*, w^*)$ denotes the velocity field due to surface waves in the presence of the background flow, with $\mathbf{u}^*$ and w^* the velocity vector in the horizontal plane and vertical component, respectively, $\mathbf{x}^*$ the position vector in the horizontal plane, and t^* is time; P^* denotes the total pressure; ρ and g denote the fluid density and gravitational acceleration, respectively; $\zeta^*(\mathbf{x}^*, t^*)$ denotes the surface elevation due to additional surface waves in the presence of the background flow, $\mathbf{U}_3^*$.

We choose the characteristic length L_c^* and velocity u_c^* to nondimensionalize the variables. In all cases we consider in §IV, a wave frequency spectrum $S^*(\omega^*)$ is assumed which has a clear peak at a frequency ω_p^*. Therefore, we form the characteristic length, $L_c^* = g/\omega_p^{*2}$, and, characteristic velocity, $u_c^* = g/\omega_p^*$ using g and ω_p^* for convenience while our specific choice does not affect the generality of the theory derived in §II and III. Explicitly,

$$(x^*, y^*, z^*) = (x, y, z)L_c^*; \quad t^* = \frac{L_c^*}{u_c^*}t; \quad \mathcal{V}^* = u_c^*\mathcal{V}; \tag{3a}$$

Here, $\mathcal{V}$ represents any velocity component, and we define the wave–induced nondimensional pressure as

$$P = (P^* + \rho g z^*)/(\rho u_c^{*2}). \tag{4}$$

The dimensionless continuity and Euler momentum equations become

$$\nabla_3 \cdot \mathbf{V}_3 = 0; \tag{5}$$

$$\partial_t \mathbf{V}_3 + (\mathbf{V}_3 \cdot \nabla_3)\mathbf{U}_3 + (\mathbf{U}_3 \cdot \nabla_3)\mathbf{V}_3 + \nabla_3 P = -(\mathbf{V}_3 \cdot \nabla_3)\mathbf{V}_3, \tag{6}$$

for $-\infty < z < \zeta + \eta$.

The governing equations (5) and (6) should be solved subject to the dynamic and kinematic boundary conditions at the surface, respectively,

$$P - (\zeta + \eta) = 0 \ \text{ and } w = \partial_t \zeta + (\mathbf{u} + \mathbf{U}) \cdot \nabla \zeta \ \text{ for } \ z = \zeta + \eta, \tag{7}$$

and the deepwater seabed condition

$$(\mathbf{u}, w) = 0 \text{ for } \ z \to -\infty. \tag{8}$$

B. Perturbation expansion and linear wave fields

We seek the solution for unknown velocity ($\mathbf{V}$) and elevation (ζ) of the boundary value problem described by (5) – (8) in a form of power series in wave steepness denoted by ϵ; i.e. a so-called Stokes expansion. To leading order, they are given by

$$[\zeta, \mathbf{u}, w, P] = \epsilon[\zeta^{(1)}, \mathbf{u}^{(1)}, w^{(1)}, P^{(1)}] + \epsilon^2[\zeta^{(2)}, \mathbf{u}^{(2)}, w^{(2)}, P^{(2)}], \tag{9}$$

where the terms are kept up to second order in wave steepness and the superscript '(j)' denotes the j-th order in wave steepness. Inserting the perturbed solutions (9) into the boundary value problem described by (5) – (8) and collecting the terms at the same order lead to the various boundary value problems at different orders in wave steepness.

Linear surface elevation due to irregular surface waves can be described by

$$\zeta^{(1)}(\mathbf{x}, t) = \mathcal{R}\left[\frac{1}{4\pi^2}\int |\hat{\zeta}(\mathbf{k})| \mathrm{e}^{\mathrm{i}\psi(\mathbf{k},\mathbf{x},t)} \mathrm{d}\mathbf{k}\right], \tag{10}$$

where $\mathcal{R}$ denotes the real part, $\mathbf{k}$ denotes a wavenumber vector in the horizontal plane, $\hat{\zeta}(\mathbf{k})$ denotes the linear wave elevation transformed in the Fourier $\mathbf{k}$ plane, $\psi(\mathbf{k}, \mathbf{x}, t) = \mathbf{k} \cdot \mathbf{x} - \omega(\mathbf{k})t + \theta(\mathbf{k})$

denotes the rapidly varying phase with $\theta(\mathbf{k})$ the initial phase (angle) of the complex elevation $\hat{\zeta}(\mathbf{k})$ at the origin, $\omega(\mathbf{k})$ denotes the angular frequency of wave $\mathbf{k}$. Integration is over the whole $\mathbf{k}$ plane. Without the detailed derivations, this paper employs the Direct Integration Method (DIM) developed by Li and Ellingsen [47], which provides a shear-modified dispersion relation $\omega = \omega(\mathbf{k})$. The dispersion relation is solved numerically together with the linear wave fields $\mathbf{u}^{(1)}$, $w^{(1)}$, and $P^{(1)}$.

The linear velocity and pressure in the physical plane can be obtained through an inverse Fourier transform as follows

$$\begin{bmatrix} \mathbf{u}^{(1)}(\mathbf{x},z,t) \\ w^{(1)}(\mathbf{x},z,t) \\ P^{(1)}(\mathbf{x},z,t) \end{bmatrix} = \mathcal{R}\left\{ \frac{1}{4\pi^2}\int \begin{bmatrix} \hat{\mathbf{u}}^{(1)}(\mathbf{k},z) \\ \hat{w}^{(1)}(\mathbf{k},z) \\ \hat{P}^{(1)}(\mathbf{k},z) \end{bmatrix} \mathrm{e}^{\mathrm{i}\psi(\mathbf{k},\mathbf{x},t)}\mathrm{d}\mathbf{k} \right\}. \tag{11}$$

Arbitrary linear wave fields can then be constructed by adding monochromatic components together, in the manner of Fourier transformation. We will not consider changes in mean water level herein and set $\eta = 0$ henceforth.

C. Second-order equations of motions

Inserting the solution for unknown velocity ($\mathbf{V}$) and surface elevation (ζ) in a form of power series given by (9) into the boundary value problem described by (5)–(8), collecting the terms at second order in wave steepness, and eliminating the horizontal velocity ($\mathbf{u}^{(2)}$) and pressure ($P^{(2)}$) at second order leads to the following equations

$$(\partial_t + \mathbf{U}\cdot\nabla)\nabla_3^2 w^{(2)} - \mathbf{U}''\cdot\nabla w^{(2)} = \mathcal{N}^{(2)}(\mathbf{x},z,t), \tag{12a}$$

for $-\infty < z < \zeta$,

$$(\partial_t + \mathbf{U}\cdot\nabla)^2\partial_z w^{(2)} - \mathbf{U}'\cdot(\partial_t + \mathbf{U}\cdot\nabla)\nabla w^{(2)} - \nabla^2 w^{(2)} = \mathcal{F}^{(2)}(\mathbf{x},z,t) \text{ for } z = 0, \tag{12b}$$

$$w^{(2)} = 0 \text{ for } z \to -\infty, \tag{12c}$$

where $\mathbf{U}'' = \partial_{zz}\mathbf{U}$, the forcing terms, $\mathcal{N}^{(2)}$ and $\mathcal{F}^{(2)}$, on the right hand side of (12a) and (12b) are functions of linear wave fields and are given by

$$\mathcal{N}^{(2)} = \nabla\cdot\left[(\mathbf{V}^{(1)}\cdot\nabla_3)\mathbf{u}^{(1)}\right]' - \nabla^2\left[(\mathbf{V}^{(1)}\cdot\nabla_3)w^{(1)}\right], \tag{13a}$$

$$\begin{aligned}\mathcal{F}^{(2)} = & -\nabla^2(\mathbf{u}^{(1)}\cdot\nabla\zeta^{(1)}) - [\nabla^2(\partial_t + \mathbf{U}\cdot\nabla)P^{(1)\prime} - \nabla^2 w^{(1)\prime}]\zeta - \zeta^{(1)}\nabla^2(\mathbf{U}'\cdot\nabla)P^{(1)} \\ & + (\partial_t + \mathbf{U}\cdot\nabla)\nabla\cdot[(\mathbf{V}^{(1)}\cdot\nabla_3)\mathbf{u}^{(1)}],\end{aligned} \tag{13b}$$

with notation $(\cdots)' \equiv \partial_z(\cdots)$. Inserting the linear solution from (11), the forcing term is then

$$\mathcal{N}^{(2)} = \mathcal{R}\left[\frac{1}{16\pi^4}\iint \hat{\mathcal{N}}^{(2)}(\mathbf{k}_1,\mathbf{k}_2,\mathbf{x},z,t)\mathrm{d}\mathbf{k}_1\mathrm{d}\mathbf{k}_2\right], \tag{14a}$$

$$\mathcal{F}^{(2)} = \mathcal{R}\left[\frac{1}{16\pi^4}\iint \hat{\mathcal{F}}^{(2)}(\mathbf{k}_1,\mathbf{k}_2,\mathbf{x},z,t)\mathrm{d}\mathbf{k}_1\mathrm{d}\mathbf{k}_2\right], \tag{14b}$$

where $\mathbf{k}_1$ and $\mathbf{k}_2$ denote the wave vector of two different linear wave trains; the forcing terms in the Fourier space are decomposed into the two types of second–order wave interactions as (see, e.g., [11, 66])

$$\hat{\mathcal{N}}^{(2)} = \hat{\mathcal{N}}_+^{(2)}(\mathbf{k}_1,\mathbf{k}_2,z)\mathrm{e}^{\mathrm{i}(\psi_1+\psi_2)} + \hat{\mathcal{N}}_-^{(2)}(\mathbf{k}_1,\mathbf{k}_2,z)\mathrm{e}^{\mathrm{i}(\psi_1-\psi_2)}, \tag{14c}$$

$$\hat{\mathcal{F}}^{(2)} = \hat{\mathcal{F}}_+^{(2)}(\mathbf{k}_1,\mathbf{k}_2,z)\mathrm{e}^{\mathrm{i}(\psi_1+\psi_2)} + \hat{\mathcal{F}}_-^{(2)}(\mathbf{k}_1,\mathbf{k}_2,z)\mathrm{e}^{\mathrm{i}(\psi_1-\psi_2)}, \tag{14d}$$

where the subscripts '+' or '-' denote the components for the superharmonics and subharmonics, respectively; the wave phases are denoted with shorthand: $\psi_j = \psi(\mathbf{k}_j,\mathbf{x},t)$; and the lengthy expressions of $\hat{\mathcal{N}}_\pm$ and $\hat{\mathcal{F}}_\pm$ are given in Appendix B.

With the linear velocity fields solved for by using the DIM [47], the second-order equations (12a)– (12c) for the vertical velocity $w^{(2)}$ can be solved numerically in Fourier space. Due to the interaction of different wave components and the main harmonic components of the forcing terms (i.e. $\mathcal{N}^{(2)}$ and $\mathcal{F}^{(2)}$) in the Fourier plane, the second-order vertical velocity

$$w^{(2)}(\mathbf{x},z,t) = \mathcal{R}\left[\frac{1}{16\pi^4}\iint \hat{w}^{(2)}(\mathbf{k}_1,\mathbf{k}_2,\mathbf{x},z,t)\mathrm{d}\mathbf{k}_1\mathrm{d}\mathbf{k}_2\right]. \tag{15}$$

We can also decompose $\hat{w}^{(2)}$ in terms corresponding to the two types of second–order wave interactions as

$$\hat{w}^{(2)}(\mathbf{k}_1,\mathbf{k}_2,z,\mathbf{x},t) = \hat{w}_+^{(2)}(\mathbf{k}_1,\mathbf{k}_2,z)\mathrm{e}^{\mathrm{i}(\psi_1+\psi_2)} + \hat{w}_-^{(2)}(\mathbf{k}_1,\mathbf{k}_2,z)\mathrm{e}^{\mathrm{i}(\psi_1-\psi_2)}, \tag{16}$$

Each component on the right hand side of (16) for $\hat{w}^{(2)}$ can be solved for numerically from the boundary value problem as follows

$$\hat{w}_\pm^{(2)\prime\prime} - \left(|\mathbf{k}_\pm|^2 + \frac{\mathbf{k}_\pm\cdot\mathbf{U}''}{\mathbf{k}_\pm\cdot\mathbf{U}-\omega_\pm}\right)\hat{w}_\pm^{(2)} = \frac{\hat{\mathcal{N}}_\pm^{(2)}}{\mathbf{k}_\pm\cdot\mathbf{U}-\omega_\pm}, \tag{17a}$$

for $-\infty < z < 0$, where $\mathbf{k}_\pm = \mathbf{k}_1 \pm \mathbf{k}_2$, $\omega_\pm = \omega(\mathbf{k}_1) \pm \omega(\mathbf{k}_2)$, and boundary conditions

$$-(\mathbf{k}_\pm\cdot\mathbf{U}-\omega_\pm)^2\partial_z\hat{w}_\pm^{(2)} + \left[\mathbf{k}_\pm\cdot\mathbf{U}'(\mathbf{k}_\pm\cdot\mathbf{U}-\omega_\pm) + |\mathbf{k}_\pm|^2\right]\hat{w}_\pm^{(2)} = \hat{\mathcal{F}}_\pm^{(2)}(\mathbf{k}_\pm,z) \text{ for } z=\eta, \tag{17b}$$

$$\hat{w}_\pm^{(2)} = 0 \text{ for } z\to-\infty. \tag{17c}$$

In our problem setting the waves obtained from the second-order boundary value problem (17a,b,c) are bound since they do not satisfy the linear dispersion relation and can only propagate together with their linear free contents. Moreover, with the linear free waves obtained, the second-order ordinary equation (17a) with two boundary conditions (17b,c) can be solved for numerically with a finite difference method where a central Euler approximation to the second-order derivative, $\hat{w}_{\pm}^{(2)\prime\prime}$, was used in this paper. Especially for directionally spread irregular waves in a random sea, we remark that the numerical estimation of double Fourier integrals in a form as (14a,b) is computationally expensive for statistical analysis. Nevertheless, the framework developed here can be easily reformulated such that a pseudo-spectral method for the second-order interaction of waves in a vertically sheared current can be used, following papers, e.g., [67] and [68] for a high-order spectral method and [69] for a semianalytical approach. In doing so, it allows for reducing the computational operations of $\mathcal{O}(N_g^2)$ to $\mathcal{O}(N_g \text{In} N_g)$, with N_g the total number of discrete points chosen for the grid of a computational domain.

The second-order wave surface elevation $\zeta^{(2)}$ can be obtained from the following kinematic boundary condition

$$(\partial_t + \mathbf{U}\cdot\nabla)\zeta^{(2)} = w^{(2)} + \zeta^{(1)}w^{(1)\prime} - \frac{1}{2}\mathbf{U}'\cdot\nabla\big(\zeta^{(1)}\big)^2 - \mathbf{u}^{(1)}\cdot\nabla\zeta^{(1)}, \tag{18}$$

which leads to the surface elevation $\zeta^{(2)}$ given by

$$\zeta^{(2)}(\mathbf{x},t) = \mathcal{R}\left[\frac{1}{16\pi^2}\iint \hat{\zeta}^{(2)}(\mathbf{k}_1,\mathbf{k}_2;\mathbf{x},t)\mathrm{d}\mathbf{k}_1\mathrm{d}\mathbf{k}_2\right] \text{ with} \tag{19a}$$

$$\hat{\zeta}^{(2)} = \hat{\zeta}_+^{(2)}(\mathbf{k}_1,\mathbf{k}_2)\mathrm{e}^{\mathrm{i}(\psi_1+\psi_2)} + \hat{\zeta}_-^{(2)}(\mathbf{k}_1,\mathbf{k}_2)\mathrm{e}^{\mathrm{i}(\psi_1-\psi_2)}, \tag{19b}$$

where the elevation $\hat{\zeta}_{\pm}^{(2)}$ is obtained from (18) in the Fourier plane through substituting the vertical velocity $w^{(2)}$ and the linear wave fields $\mathbf{u}^{(1)}$ and $\zeta^{(1)}$. It's noteworthy that for $\mathbf{k}_1 = \mathbf{k}_2$ the super-harmonics ($\hat{\zeta}_+^{(2)}$) reduce to the well-known second-order Stokes waves. The sub-harmonics ($\hat{\zeta}_-^{(2)}$) become a constant, which refers to a mean water level and is ignored in our experiment.

D. Notation in the frequency domain

The theory in §II so far was formulated in reciprocal horizontal ($\mathbf{k}$) space. Often it is more convenient in practice to use a frequency domain formulation, for instance when working with power spectra, from time series from wave buoys, say. In the presence of a vertically sheared current the dispersion relation $\omega = \omega(\mathbf{k})$ is anisotropic in any reference system, i.e., ω is always a function of the direction of $\mathbf{k}$, not only its modulus. This introduces subtleties in interpreting nondirectional wave frequency data in the presence of a sheared current as wavelength cannot be inferred from frequency alone. We herein work in two dimensions, i.e., waves propagating with known direction either along or against the current, thus eschewing this potential complication.

The linear and quadratic-order elevations are denoted

$$\zeta^{(1)}(\mathbf{x},t) = \mathcal{R}\left(\int a(\omega)\mathrm{e}^{\mathrm{i}\psi}\mathrm{d}\omega\right), \tag{20a}$$

$$\zeta^{(2)}(\mathbf{x},t) = \mathcal{R}\left\{\iint a_1a_2\left[\hat{A}^{+}_{12}\mathrm{e}^{\mathrm{i}(\psi_1+\psi_2)} + \hat{A}^{-}_{12}\mathrm{e}^{\mathrm{i}(\psi_1-\psi_2)}\right]\mathrm{d}\omega_1\mathrm{d}\omega_2\right\}. \tag{20b}$$

where $a(\omega)$ denotes the linear (real) amplitude of a wave with frequency ω and complex phase $\psi(\omega) = \mathbf{k}\cdot\mathbf{x} - \omega t + \theta(\omega)$, where we solve the dispersion relation $\omega = \omega(\mathbf{k})$ for the wave vector with a given frequency using the DIM method as noted. The following notations are used: $a_n = a(\omega_n)$, $\psi_n = \psi(\omega_n)$, $\hat{A}^{\pm}_{12} = \hat{A}^{\pm}(\omega_1,\omega_2)$ with

$$\hat{A}^{\pm}(\omega_1,\omega_2) = \frac{|\hat{\zeta}^{(2)}_{\pm}(\omega_1,\omega_2)|}{a_1a_2}, \tag{20c}$$

where $\hat{\zeta}^{(2)}_{\pm}$ was given by (19b) with the difference that it is expressed here in the frequency domain instead.

III. WAVES OF A NARROW BANDWIDTH

In this section we present the skewness and probability density function of the surface displacement and wave crests in the special case where the bandwidth of the wave spectrum is narrow. We now use the frequency-domain formulation of §II D. Consider an ensemble of waves described in the form (20) where the amplitude $a(\omega)$ becomes an independent random variable denoted by $\tilde{a}(\omega)$ which follows a Rayleigh distribution based on a spectrum $S(\omega)$ and where the phase θ becomes another independent random variable, $\tilde{\theta}$, which is uniformly distributed in the range $[0,2\pi\rangle$. Therefore, $\zeta(\mathbf{x},t)\to\tilde{\zeta}(\tilde{a}(\omega),\tilde{\theta}(\omega))$. The j-th spectral moment m_j is defined as

$$m_j = \int \omega^j S(\omega)\mathrm{d}\omega;\quad j\in\{0,1,2,...\}. \tag{21}$$

Assuming zero mean water level as before, the standard deviation, σ, and skewness, λ_3, of the surface elevation are

$$\sigma = \sqrt{\langle\tilde{\zeta}^2\rangle}\ \text{ and }\ \lambda_3 = \langle\tilde{\zeta}^3\rangle/\sigma^3, \tag{22a,b}$$

where $\langle...\rangle$ denotes the expectation value of random variables. Assuming the energy spectrum $S(\omega)$ to have a narrow bandwidth ($\nu = \sqrt{1-m_2^2/(m_0m_4)} \ll 1$), we follow the detailed derivations of Fedele and Tayfun [23] using the elevations (20a,b), and obtain to $\mathcal{O}(\epsilon)$

$$\sigma^2 = m_0 \text{ and } \lambda_3 = 6\sigma\hat{A}^{+}_{mm}, \tag{23a,b}$$

where $\hat{A}^+_{mm} = \hat{A}(\omega_m, \omega_m)$ denotes the second-order superharmonic amplitude of the spectral mean wave, with ω_m the spectral mean frequency given by

$$\omega_m = m_1/m_0. \tag{24}$$

The skewness given by (23b) agrees with Fedele and Tayfun [23], Srokosz and Longuet-Higgins [70] and Li *et al.* [10] for waves in the absence of a shear current, which is clear when noting that the superharmonic amplitude $\hat{A}^+_{mm}$ can be written as $k_m/2 \equiv \omega_m^2/(2g)$ in the case for second-order deepwater Stokes waves (see, e.g., [11]). It is different from Fedele and Tayfun [23] to the extent that it does not account for the effect of bandwidth as it is not so straightforward due to a shear current. Nevertheless, it allows us to take into account the effect of a shear current to some extent. Especially, if all linear waves follow the same power energy spectrum with a narrow bandwidth, i.e., m_j are identical for all cases, the spectral mean given by (24) is identical regardless of a shear current. A shear current affects the skewness given by (23b) through the second-order superharmonic amplitude of the spectral mean wave, compared with the cases in the absence.

Following Longuet-Higgins [12], we obtain that the normalized surface displacements follow the distribution

$$p_\zeta(\tilde{\zeta}) = \frac{1}{\sqrt{2\pi}} \mathrm{e}^{-\tilde{\zeta}^2/2} \left[1 + \frac{\lambda_3}{6}\tilde{\zeta}(\tilde{\zeta}^2 - 3)\right]. \tag{25}$$

For linear waves, where $\lambda_3 = 0$, expression (25) becomes a Gaussian distribution. Different from Longuet-Higgins [12], the probability density function given by (25) can account for the effect of a shear current due to that the skewness λ_3 is modified according to (23b) which considers the effect of a shear current.

Similarly, following Forristall [17], the 'exceedance probability', i.e., the probability that a randomly chosen wave crest X_c exceeds the value $\tilde{\zeta}_c$, is found as

$$P(X_c > \tilde{\zeta}_c) = \exp\left[-\frac{1}{8(\hat{A}^+_{mm}\sigma)^2}\left(\sqrt{1 + \frac{16\tilde{\zeta}_c}{H_s}\hat{A}^+_{mm}\sigma} - 1\right)^2\right], \tag{26}$$

where H_s is the significant wave height. The exceedance probability given by (26) agrees with (2.12) by Li *et al.* [10] with the same chosen notations whereas the main difference lies in that the effect of a shear current enters here via the superharmonic amplitude of the spectral mean wave, $\hat{A}^+_{mm}$. In the limit of infinitesimal wave, i.e., $m_0 \to 0^+$, the exceedance probability of wave crest becomes

$$P(X_c > \tilde{\zeta}_c) = \exp\left(-8\frac{\tilde{\zeta}_c^2}{H_s^2}\right), \tag{27}$$

which is the Rayleigh distribution as expected. For second-order deepwater Stokes waves in the absence of a shear current which admits $\hat{A}^{+}_{mm} = k_m/2 \equiv \omega_m^2/(2g)$, the exceedance probability given by (26) is identical to eq.(4) in Forristall [17]. We will refer repeatedly to (25) and (26) in section V B.

IV. NUMERICAL SETUP

In our simulations, we generate two-dimensional (long-crested or uni-directional) waves from realistic spectra. Doing so implies that the possible triad resonant interactions in three dimensions considered in previous papers, e.g., [38, 58, 71] are assumed negligible in the simulations. We choose the characteristic velocity, $u_c^* = g/\omega_p^*$, as defined in §II A. Here, ω_p^* is the peak frequency of the spectrum; although $\omega_p = 1$ by definition, we find it instructive to retain it in some equations below.

We begin by defining the terms following and opposing shear for two-dimensional flow, i.e., where all waves propagate parallel or antiparallel to the mean current. We will assume that waves travel along the positive x axis. We then define

- Following shear: $U'(z) < 0$;
- Opposing shear: $U'(z) > 0$.

Following (opposing) shear corresponds to the situation where the flow increases (decreases) in the direction of propagation with increasing depth.

Note carefully the distinction between following (opposing) shear and following (opposing) current. When seen in an Earth–fixed reference system, currents in nature are often strongest near the surface and decrease to zero at larger depths, such as in the Columbia River Mouth current we regard in section V E. In such a case a “following surface current” $U(z) > 0$ would correspond to opposing shear and *vice versa*. For clarity of comparison between cases we shall work in a surface-following frame and, therefore, assume $U(0) = 0$, in which case following shear implies positive $U(z)$ for a monotonically varying U. Doing so allows us to focus only on the effects due to the profile shear and curvature of a current.

A. Realisation of random seas states for linear waves

We follow Tayfun [13] and Tucker *et al.* [65] for the realisation of random sea states, which assumes Rayleigh distributed amplitude of linear waves and uniformly distributed wave phases in the range of $[0, 2\pi\rangle$. The energy spectrum we choose for computation is JONSWAP spectrum

[72] with a peak enhancement (or peakedness) parameter of $\gamma = 3.3$ and moderately narrow bandwidth[73, 74], which is shown in figure 1(a).

The JONSWAP spectrum is given by (recall that $\omega_p = 1$)

$$S_J(\omega) = \frac{\tilde{\alpha}_J}{\omega^5} \exp\left[-1.25\omega^{-4}\right] \gamma^{b(\omega)}, \tag{28}$$

where the peak enhancement factor γ appears with an exponent

$$b(\omega) = \exp\left[-\frac{(\omega-1)^2}{2\sigma_J^2}\right], \tag{29}$$

and

$$\sigma_J = \begin{cases} 0.07, & \omega \le 1 \\ 0.09, & \omega > 1. \end{cases} \tag{30}$$

The parameter $\tilde{\alpha}_J$ is chosen such that the JONSWAP spectrum is fixed for all numerical cases, i.e., independent of a current profile. The frequency is truncated at $0.01\omega_p$ and $2.6\omega_p$. The bandwidth parameter is defined as

$$\nu = \sqrt{1 - \frac{m_2^2}{m_0 m_4}} \tag{31}$$

and here $\nu = 0.5284$. For another widely used bandwidth parameter $\nu_L = \sqrt{m_0 m_2/m_1^2 - 1}$ proposed by Longuet-Higgins [75], the value becomes 0.2689. We choose bulk steepness $\epsilon = \frac{1}{2}H_s = 0.14$ in all cases. As noted, the peak frequency ($\omega_p = 1$), significant wave height (H_s), and the moments (m_j) of the JONSWAP spectrum are fixed for all cases, regardless of the profile of a shear current. However, the spectrum peak wavenumber $k_p \equiv k(\omega_p) = k(1) \neq 1$ in the presence of a current, since the linear dispersion relation $k(\omega)$ depends on $U(z)$, as explained in §II and §III.

Once the input spectrum is determined, the amplitudes a_i of a total of N_s linear elementary waves are generated with a prescribed significant wave height, with

$$\sum_{i=1}^{N_s} \frac{\tilde{a}_i^2}{2} = \int_\omega S(\omega)\mathrm{d}\omega \text{ and } \zeta^{(1)}(x,t) = \sum_{i=1}^{N_s} \tilde{a}_i \cos(k_i x - \omega_i t + \tilde{\theta}_i), \tag{32}$$

where the energy spectrum is discretised with unequal frequency intervals and an identical area of N_s energy bins (i.e., constant $S(\omega_i)\mathrm{d}\omega_i$). For a train of random waves, we assume the amplitude $\tilde{a}_i$ follows a Rayleigh distribution and the phase $\tilde{\theta}$ a uniform distribution in the range $[0, 2\pi\rangle$ similar to §III and Tayfun [15]. The wave numbers k_i are found numerically from ω_i using the DIM algorithm as described. We especially computed the temporal evolution of the linear surface elevation at $x = 0$ and then, the second-order correction of the wave surface are calculated from (19a) and (19b).

We also make a flow diagram of numerical implementations, which is shown in Appendix A. In our simulations, 128 elementary waves are generated from the relevant input wave spectra and ran from $0 \leq t \leq 5638$. 2000 realizations were simulated to assure that the skewness of the wave surface elevation was converged.

B. Current profiles and cases considered

We consider three different current profiles with different parameters, which are typical of the open ocean, including an exponential profile, a linearly sheared current, and one that was measured at the mouth of Columbia River from Zippel & Thomson [54], as shown in figure 1(b) and (c).

1. Model profiles

The exponential and linear profile of shear current are parameterized as

$$\mathbf{U}_{\text{exp}}(z) = \beta[\exp(\alpha z) - 1]\mathbf{e}_x \text{ and } \mathbf{U}_{\text{lin}} = Sz\mathbf{e}_x, \tag{33a,b}$$

respectively, where $\mathbf{e}_x$ is a unit vector along the positive x axis, the subscripts 'exp' and 'L' denote the exponential and linear profile, respectively, α ($\alpha > 0$), β, and S are dimensionless parameters that define the magnitude and shear strength of a current profile relative to the peak wave parameters. Note that we choose a reference system following the free surface so that $\mathbf{U}(0) = 0$. This eschews arbitrary Doppler shift terms which would clutter the formalism, reduces the number of free parameters, and makes results from different profiles immediately comparable. The choice also emphasizes that it is the shear $U'(z)$ and curvature $U''(z)$ which cause statistics to be altered, not the strength of the current itself. The surface shear is obtained from (33)

$$\mathbf{U}'_{\text{exp}}(0) = \alpha\beta\mathbf{e}_x \text{ and } \mathbf{U}'_{\text{lin}}(0) = S\mathbf{e}_x, \tag{34a,b}$$

which denote the profile shear of an exponential and linearly sheared current at still water surface, respectively.

Recall that following (opposing) shear correspond to $U'(z) < 0$ (> 0). We wish our model current to have strong, but not unreasonable vertical shear. To determine how strongly the current shear affects the dispersion of a wave of wave number k^* or frequency ω^* (whichever is known),

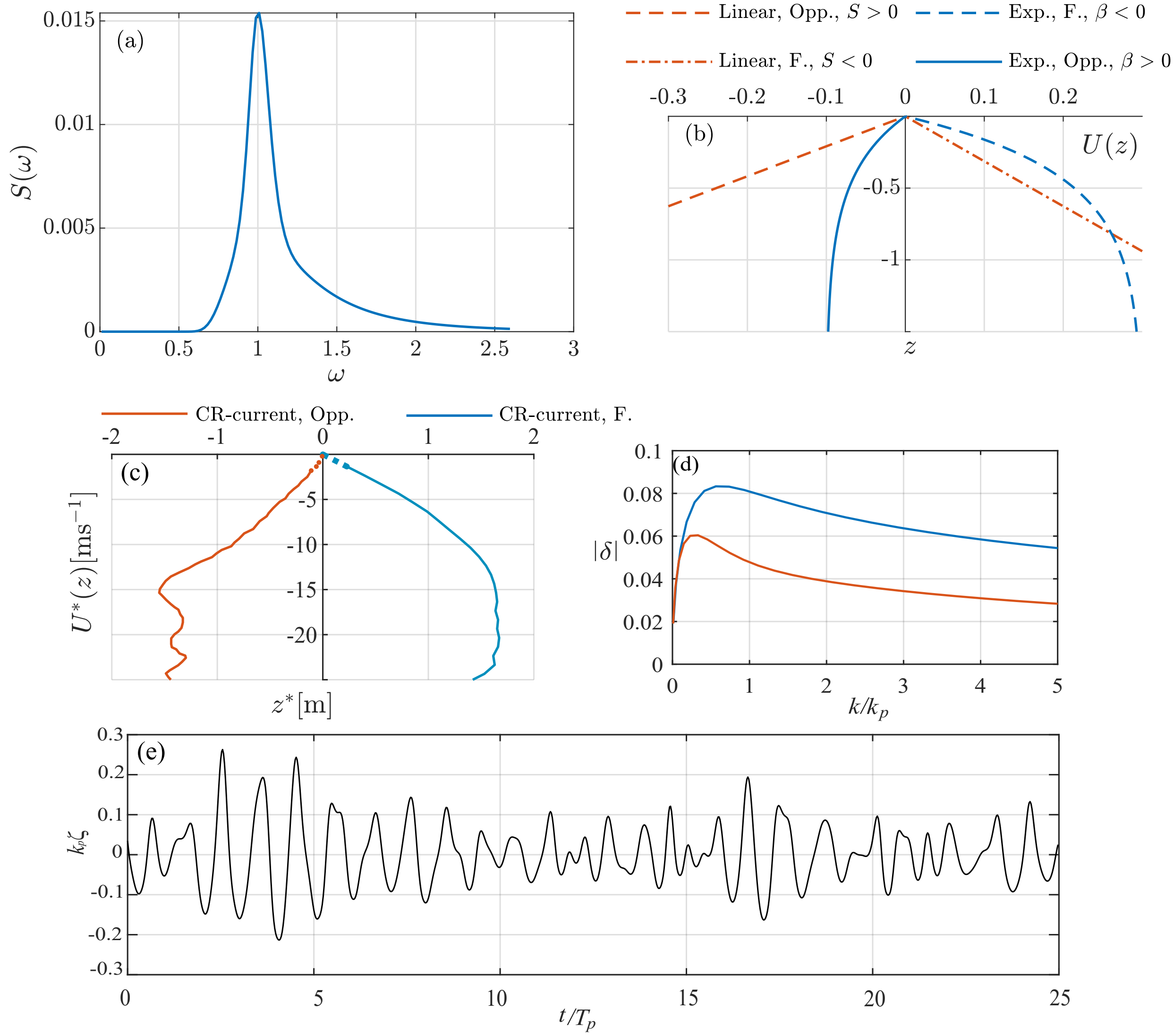

FIG. 1. (a): JONSWAP power energy spectrum of linear waves with nondimensional peak frequency $\omega_p = 1$ and bulk steepness $\epsilon = 0.14$; (b) examples of linear and exponential ('Exp.') shear profiles where both opposing ('Opp.') and following ('F.') shear are shown; (c) two tidal current profiles from ref. Zippel and Thomson [54] mearured at the mouth of Columbia river ('CR'), during ebb tide (following shear, 'F.'), and flood (mostly opposing shear, 'Opp.'), respectively. Note that in an Earth-fixed coordinate system (see Fig. 3 of [54]) these correspond to opposing and following surface currents, respectively. Dashed lines are extrapolations from $z = 1.35\,\mathrm{m}$ to the surface; (d) wave–averaged shear $|\delta(k)|$ for the two profiles in panel c; (e) extract of the time series of wave surface elevation for illustration, here without current.

the proper parameter to consider is the wave–weighted depth-averaged shear [60], respectively

$$\delta = \frac{1}{c_0^*}\int_{-\infty}^{0} U^{*\prime}(z^*)\mathrm{e}^{2k^*z^*}\mathrm{d}z^* = \sqrt{k}\int_{-\infty}^{0} U'(z)\mathrm{e}^{2kz}\mathrm{d}z \tag{35}$$

nondimensionlized as explained in Section II A, and $c_0^* = \sqrt{g/k^*}$. Inserting $U'(z) = \alpha\beta\exp(2\alpha z)$

gives

$$|\delta| = \frac{|\alpha\beta|\sqrt{k}}{\alpha + 2k}, \tag{36}$$

whose maximum value is found at $k = \alpha/2$ and in either case, $|\delta|_{\max} = |\alpha\beta|/\sqrt{8}$. In the following sections we use $\alpha = 2.5$ and $|\beta| \leq 0.3$ giving $|\delta|_{\max} \lesssim 0.17$.

2. Profile from the Mouth of Columbia River

The profiles of tidal currents in the Mouth of the Columbia River have been used as a test-case in a wide array of studies of wave-shear current interactions (e.g. [46, 47, 54, 76–80]) due to the availability of high quality current profile measurements [54, 64] and strong vertical shear. Herein we use the profiles measured by Zippel and Thomson [54] using an acoustic Doppler current profiler (ADCP) mounted on a drifter. The currents were measured between 1.35 m and 25 m depth, but we require profiles ranging all the way to the undisturbed surface level. What the profile might look like in the top 1.35 m is not obvious; the shear strength can drop sharply closer to the surface [81], but could also increase all the way to the top centimetres [62]. We use a polynomial extrapolation as shown in figure 1c; we show in appendix D that two other common approaches produce no discernable difference in the resulting skewness. The current profiles reported in Zippel and Thomson [54] and shown in figure Fig. 8a are fitted with a 7th order polynomial to the surface. The wave-averaged dimensionless shear δ of Eq. (35) for the two profiles in Fig. 1c are seen in Fig. 1d, peaking near 0.095 for the following current.

Note that the currents taken from Zippel and Thomson [54] are not extreme for the location — the shear current used in e.g. Li *et al.* [82] taken from the measurements during the RISE project [64] peaks at a value $\delta \approx 0.19$, more than our strongest exponential model current. For comparison with the results of Zippel and Thomson [54] for ebb and flow respectively, we choose the more conservative profiles in the latter.

We remark that Zakharov and Shrira [58] proposed a set of analytical theory for second-order wave-shear current problem with the assumptions $U' < 0$ and $U_{\max}/c \ll 1$. Here, $U_{\max}$ and c refer to the maximum velocity of shear current and phase velocity of surface wave, respectively. From Fig.1c the parameter $U_{\max}/c$ of Columbia River current for peak wave could reach 0.2. Hence, the theory by Zakharov and Shrira [58] is not expected to be quantitatively accurate for the Columbia River current cases considered herein.

V. RESULTS

We present second order statistical quantities for waves on model shear currents, generalising a number of classical results. The example for time series of wave surface elevation is shown in Fig. 1(e). All the statistical quantities are based on very long time series.

A. The distribution of wave surface elevation

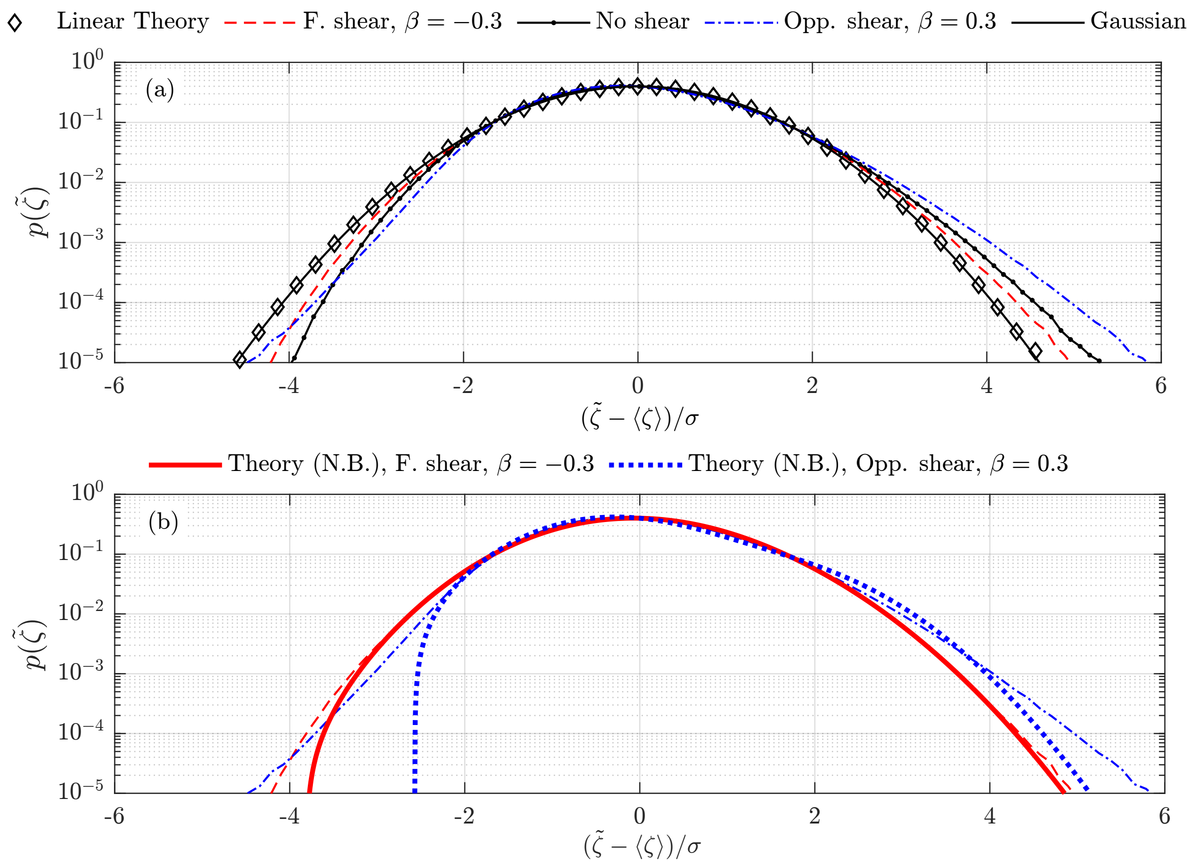

FIG. 2. Probability density function (PDF) of wave surface elevation for a moderately narrowband Gaussian input spectrum assuming the exponential current profile (33a) with β the magnitude of the shear at a still water surface. Numerical results for $\beta = -0.3$ (following shear, 'F. shear') and $\beta = 0.3$ (opposing shear: 'Opp. shear') are compared to (a) the linear prediction and the case without current, and (b) the narrowband (N.B.) theory based on (25).

In this section we examine the effects of sub-surface shear on the distribution of surface elevation to second order in steepness. We compare the case of no current to cases with following and opposing shear. We also show comparisons of the same case with shear between the broadband

and narrow-band theory presented in §II and §III, respectively. A moderately narrowband spectrum is considered, with the linear wave field amplitudes chosen from a Gaussian distribution with zero mean and variance σ^2.

Fig.2 plots the numerically calculated PDFs of wave surface elevation in the presence of a model current (equation (33)a) varying exponentially with depth, comparing our numerical results based on the broad-band theory presented in §II, together with different theoretical predictions: a Gaussian distribution, and theoretical predictions based on a narrow-band assumption presented in §III. We firstly discuss the results shown by Fig.(2a). When both second-order corrections and shear are omitted, the numerically calculated PDF (diamond symbols) should coincide with the Gaussian input distribution (zero mean, variance σ^2) which indeed it does, as expected. The probability of amplitudes greater than about two standard deviations from the mean are decreased for negative values (deep troughs) and increased for positive (high crests), conforming with the known properties of second-order Stokes waves: the wave crests get higher and wave troughs get flatter.

The presence of opposing shear $U'(z) > 0$ enhances the wave crests and flatten the wave troughs compared to no current, while following shear current has the opposite effects. The effect on second–order statistics from the shear is considerable in the range of larger wave crests ($> 2\sigma$) but modest for wave troughs (negative elevation) in this case.

A comparison of the probability density function of surface elevation for the cases in the presence of shear is shown in Fig.(2b) comparing the numerical results based on the full theory of §II and the narrow-band approximation in §III. It is seen that the narrow-band assumption agrees with the broad-band theory up to three and two standard deviations for the cases with following ('F. shear') and opposing shear ('Opp. shear'), respectively; for following shear the approximation would be good enough for most practical purposes, except extreme statistics. The narrow-band approximation underestimates the probability of the most extreme events in both cases, but to very varying degrees as the figure shows.

B. The distribution of wave maxima and crest height

The crest height is conventionally defined as the highest surface elevation reached inside discrete time intervals. Within each time interval, the surface elevation is above the mean–surface level, $\zeta > 0$, i.e., delimited by consecutive zero crossings $\zeta(t) = 0$ so that $\zeta'(t) > 0$ (< 0) at the beginning (end). This contrasts, in general, with a *surface elevation maxima* ζ_m, which is any point where

$\zeta'(t) = 0$ and $\zeta''(t) < 0$. Surface elevation maxima can be negative for a broad-band spectrum, whereas for a sufficiently narrow spectrum, the two are positive and coincide: every maximum is also a wave crest.

As discussed by Goda [83, Chapter 2], when the spectrum is not narrow there is no universal and unique definition of wave height in a time series. The most common definition based on zero-crossings described above is theoretically somewhat unsatisfactory in a broadband setting; a more theoretically coherent method proposed by Janssen [5, 84] based on the envelope of ζ is also in use [85]. For theoretical derivations the envelope procedure becomes more cumbersome for weakly non-linear waves, requiring expressions for third and fourth statistical moments, needed to adequately describe a generic wave distribution. In the following we use the customary definition using zero-crossing, as described above, bearing in mind that the identification of individual waves, and hence its distribution of maxima, will carry some dependence on the spectral shape which vanishes in the narrow-band limit.

For a narrow frequency spectrum according to linear theory, the dimensionless wave crest heights $\tilde{\zeta}_c$, normalised by significant wave height H_s, is distributed according to the Rayleigh probability function as given by (27). It is difficult, however, to determine theoretically the probability distribution of crest heights if the waves have a broad frequency spectrum. Hence, Cartwright and Longuet-Higgins [86] made a compromise by calculating the distribution of surface elevation maxima denoted by ζ_m, adapting the theory of Rice [87] from in electrical signal processing to an ocean waves setting. Their result based on linear theory for a broadband spectrum is

$$p(\xi) = \frac{1}{\sqrt{2\pi}}\nu \exp\left(-\frac{\xi^2}{2\nu^2}\right) + \frac{\xi\sqrt{1-\nu^2}}{2}\exp\left(-\frac{1}{2}\xi^2\right)\left[1 + \mathrm{erf}\left(\frac{\xi\sqrt{1-\nu^2}}{\sqrt{2}\nu}\right)\right], \tag{37}$$

where $\xi = \zeta_m/\sigma$ denotes the normalised maxima, the bandwidth parameter ν is defined in (31), m_j is the j-th moment of the energy spectrum given by (21), and erf is the error function.

Fig. 3 shows the PDF of the surface elevation maxima for linear and nonlinear results. We also plot the theoretical estimates with (37), which is given by solid line in the figure. When nonlinear effects and shear are both omitted, the numerically calculated PDF (diamond symbols) should coincide with equation (37), which indeed it does as the figure shows. The second-order results show increased probability of large wave maxima in all cases. Notice that negative-valued surface maxima occurs for a broadband spectrum, corresponding to nonzero $p(\xi)$ for $\xi < 0$. The probability of a negative maxima increases monotonically with bandwidth parameter ν.

The most prominent nonlinear effect in Fig. 3 is for opposing shear, where probability for large maxima above approximately two standard deviations is enhanced in our simulation, whereas

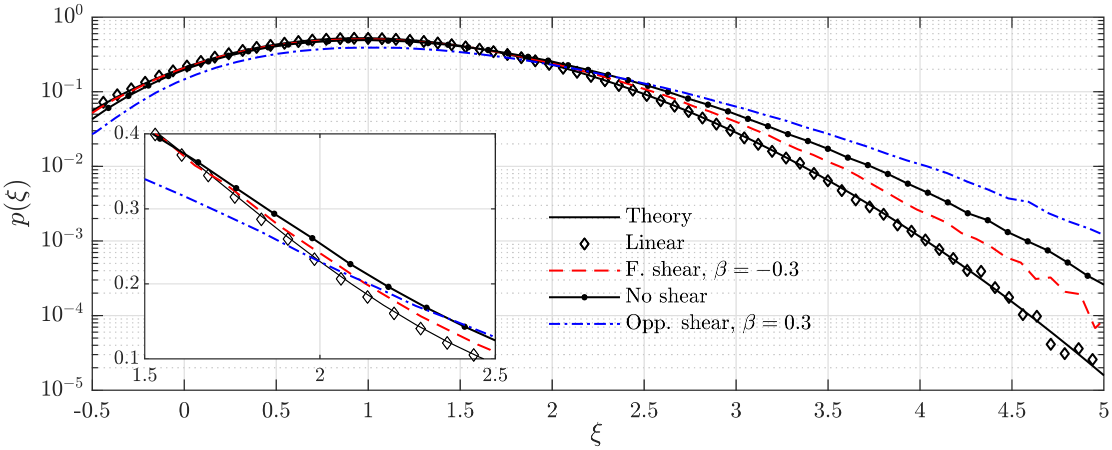

FIG. 3. Probability density function of the dimensionless maxima ($\xi = \zeta_m/\sigma$) of the wave elevation. The theoretical estimates ('Theory') are based on (37) and the other cases shown are the same as Fig.2a.

maxima below this threshold are made less probable. The current with following shear has the opposite influence. This phenomenon is consistent with the PDF of wave surface elevation studied in §V A.

There exists a few commonly used expressions for crest height distribution obtained by empirical fitting, theoretical considerations or parameterization [17, 23, 88–92]. One example we use in this section is the distribution derived by Tayfun [14] for a narrow-band spectrum, which corresponds to our narrow-band equation (26) in the limiting case of no current, i.e., $k_m^* \to k_{m0}^* = \omega_m^{*2}/g$ (shear-free dispersion relation in nondimensional units). To the best of our knowledge, theoretical expressions for wave crest distribution with a broad-band frequency spectrum have not been reported.

Fig. 4 shows the numerical PDF and exceedance probability of the scaled crest height compared to the Rayleigh and Tayfun distributions. Notice in Fig. (4a) that for very low crests $\tilde{\zeta}_c \lesssim 0.1H_s$ the probability density of wave crest height deviates noticeably from the Rayleigh curve, consistent with Fig. 3. The reason is that finite bandwidth allows negative maxima (hence a finite probability density at zero crest height), whereas the narrow-band Rayleigh distribution only allows positive maxima. The physical significance of this difference is perhaps not so high being primarily a result of the definition of a crest, referring somewhat arbitrarily to the mean water level. The tail of our numerical results without shear still agrees well with those produced by the Rayleigh distribution [23], perhaps surprising in light of the linear theory for broadband waves due to Cartwright and Longuet-Higgins [86]. This can be explained by noting that in the context of their theory our spectrum is still relatively narrow, since the bandwidth parameter $\nu \approx 0.53$ as defined in Eq. (31) is considerably smaller than unity.

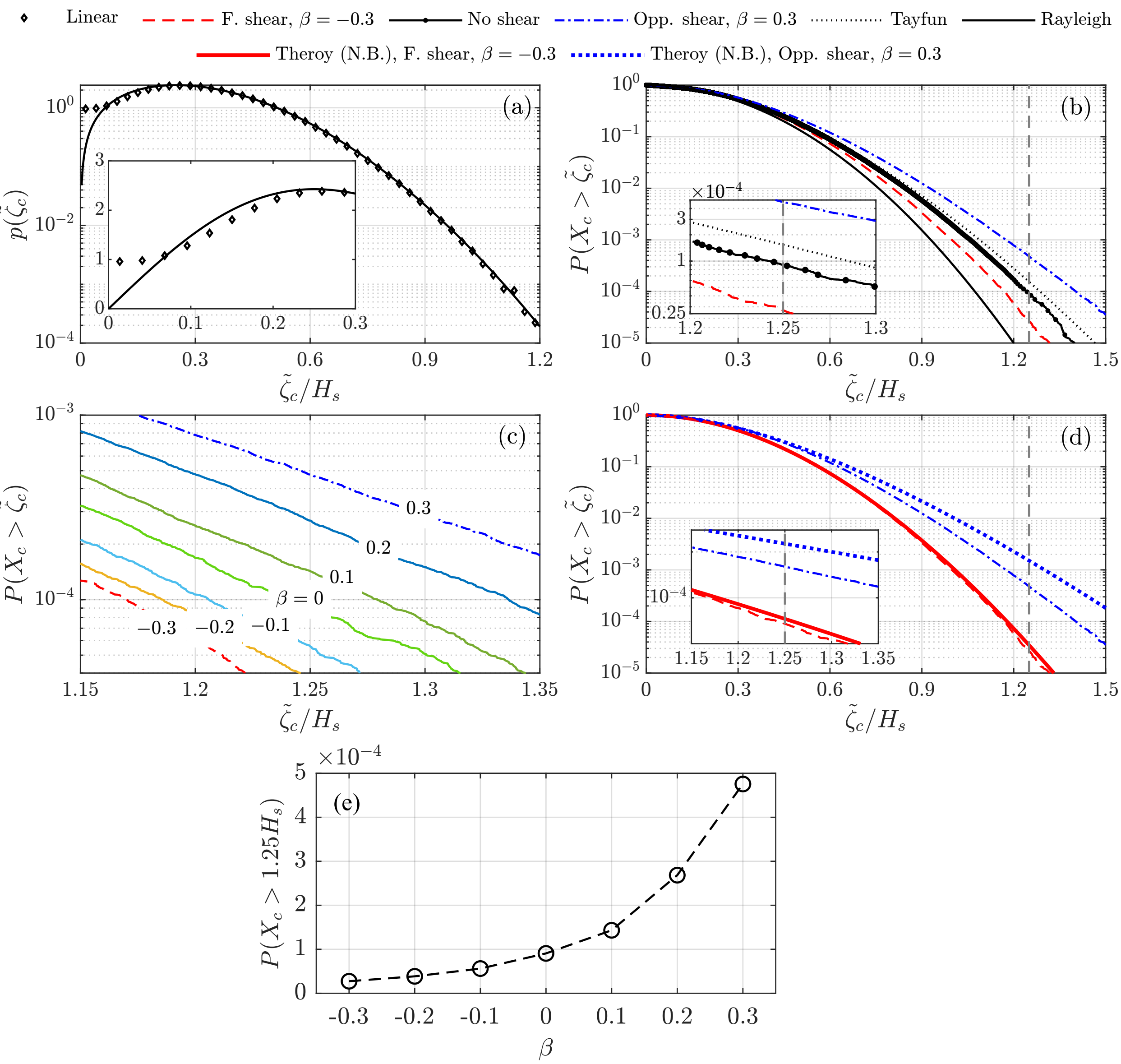

FIG. 4. Numerically calculated probability density function (panel (a)) and exceedance probability (panels (b,c,d)) for wave crests. An exponential shear profile, Eq. (33a), was assumed. (a) Linear waves based on numerical simulations and the Rayleigh probability density function; (b,c) nonlinear wave fields for varying shear strength; (d) the broad-band and narrow-band results for cases with shear based on the theory in §II and §III, respectively. We used (26) with $\beta = 0$ for the Tayfun distribution. (e) Occurrence probability of rogue wave for all the exponential shear cases in panel c.

It can be observed in Fig. 4b and 4c that, when nonlinear second–order corrections are accounted for, the tail of the simulated curve for the case with no shear clearly exceeds the Rayleigh distribution values, yet remain lower than the Tayfun distribution curve. This observation was also made by Fedele & Tayfun [23] who considered broadband waves without current; They showed that in that case the Tayfun distribution is an upper bound for the wave crest distribution to second order in steepness.

With the additional presence of a shear current and broader spectrum, crest distributions can clearly exceed that of Tayfun. The numerical results show substantial differences between the three currents considered, consistent with the general trend observed before: opposing shear makes high crests more probable and *vice versa*. The gray dashed vertical line in Fig. 4 refers to the conventional criterion for rogue waves, which is $\tilde{\zeta}_c/H_s = 1.25$ [93]. Compared with the no-shear current case, the opposing shear current leads to significant enhancement in the occurrence probability of rogue wave, as shown in Fig. 4e. The presence of following shear current has the opposite influence. The exceedance probability increases monotonously as a function of the shear strength β, which is shown in Figure (4b,c).

We note in passing, however, that whereas the probability of *unusually high* (rogue) waves is decreased on following shear, the significant wave height itself will often be increased. A typical situation where this occurs is when the shear current, measured in a land-fixed reference system, has its greatest velocity at the surface. In this case the current itself is opposing in an earth-fixed frame of reference, so waves generated elsewhere will steepen as they encounter the current. Thus the expectation in many real scenarios would be that following shear makes for rougher seas overall, whereas with opposing shear, while calmer on the whole, have an increased probability of *surprisingly* high crests. This point was discussed in depth by Hjelmervik & Trulsen [30].

Fig. 4d compares the exceedance probability of wave crest between the narrow-band predictions and numerical results for the cases with a shear current, the former of which are obtained by using (26). We observe that the narrow-band assumption leads to a small and large overestimate of the occurrence probability of wave crest for the case with a following and opposing shear current, respectively. The differences for the following current are nearly negligible, as being consistent with Fig.2b, but are much more pronounced for the opposing shear case. Fig. 4d suggests aligned conclusion with Fedele and Tayfun [23] in which it is stated that the narrow-band assumption would produce an upper bound of the exceedance probability of wave crest as aforementioned. Since the effect of current shear on waves depend on both the shift in wavelength as reflected from the linear dispersion relation as well as the amplitude of the second-order superharmonic bound waves, the overall effect of current on waves of a broad-band spectrum will in general differ in a non-trivial way from that only on the amplitude of the spectral mean wave, $\hat{A}^{+}_{mm}$. As a result, the assumption of narrow bandwidth seems to lead to larger overestimate for opposing shear compared to the case of a following shear.

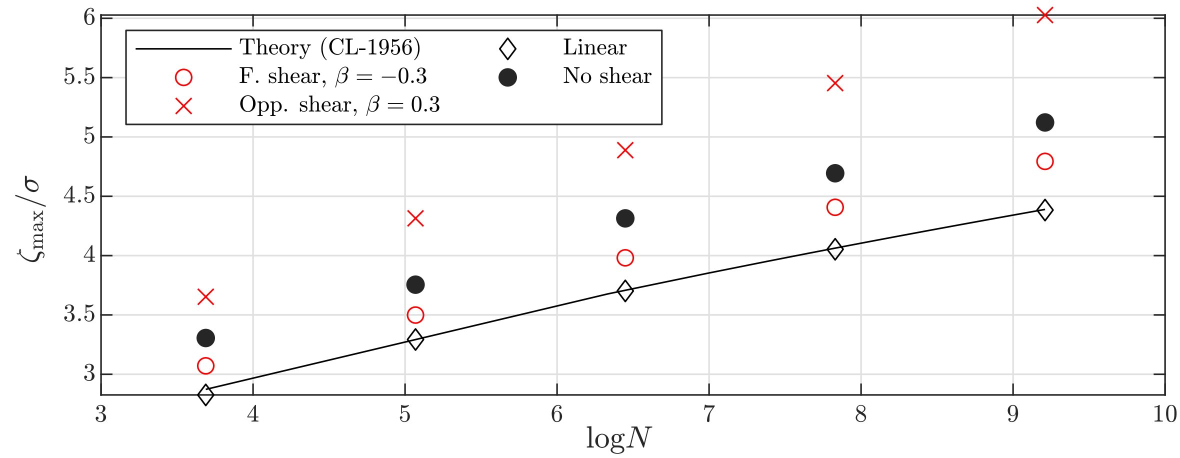

FIG. 5. The average of crest height of scenes containing the largest N waves. In the figure, the theoretical predictions (the black solid line) are based on (38) for linear waves.

C. The distribution of maximum wave crest

Consider next the distribution of the height of the highest wave crest among a randomly chosen sequence of N consecutive waves, where a ‘wave’ in this context is a time interval wherein the surface elevation contains one maximum and one minimum. A long time ago Longuet-Higgins [94] derived an expression for maximum wave crest distribution based on linear waves with a narrow band frequency spectrum. Cartwright and Longuet-Higgins [86] extended the theory to allow for a broadband spectrum, still in the linear wave regime. More recently, the Gumbel distribution was used to solve this problem up to second order [74, 92, 95]; for a linear narrow-band process, the expressions in these references are the same. In this section we use the expression from Cartwright and Longuet-Higgins [86] for comparison:

$$\frac{\zeta_{\max}}{\sigma} = \sqrt{2\ln\left[(1-\nu^2)^{\frac{1}{2}}N\right]} + \gamma_E/\sqrt{2\ln\left[(1-\nu^2)^{\frac{1}{2}}N\right]}, \tag{38}$$

where $\zeta_{\max}$ is the maximum crest height from a continuous wave train, $\gamma_E \approx 0.5772$ is Euler's constant.

Fig. 5 gives the comparison of largest crest height between our numerical results and equation (38). Each point is obtained as follows: a time series containing 2×10^6 waves is divided into 160 segments. From each segment a sequence of N consecutive waves is chosen randomly from which the highest crest is found, then the average is taken over all the highest crests and plotted in the figure. Fig. 5a shows that, once again, our simulated results of linear wave fields fit well with the theoretical solution.

Compared with linear results, second order correction makes a considerable contribution to largest crest heights. The largest crest heights rise by around 10% to 20%. A similar phenomenon was observed by Socquet-Juglard *et al.* [74], who used a narrow-band frequency spectrum and found the largest crest heights of nonlinear wave field increased by about 20% compared with linear wave fields. Moreover, it is clear that the additional presence of sub-surface shear also has notable influence on largest crest heights. The opposing and following shear current increase or decrease the largest crest heights by about 18% or 8%, respectively for the case with $\beta = 0.3$ and $\beta = -0.3$, compared with the case with no shear current. Note that the comment at the end of the previous section still applies: the current will often change a free wave surface in such a way that in absolute terms, the crest heights are actually increased by opposing shear, which is a following current in the earth-fixed frame of reference, and *vice versa*.

D. Skewness

In this section, we discuss the influence of a shear current on skewness, which is a measure of the lack of symmetry. Unlike skewness, kurtosis is not expected to be well approximated by second-order theory, and therefore not included in this paper.

Skewness of second-order waves can be expressed as a function of wave steepness, which is given by equation (23) in the limiting case of a narrow-band wave spectrum. The skewness should generally depend on both the bandwidth parameter (ν) and spectrum shape, as has been shown by Srokosz and Longuet-Higgins [70].

We consider two types of shear currents, as given in equations (33a,b). From the point of view of the waves, which can "feel" the current only down to about half a wavelength's depth, the significant difference is that a linear current has the same shear at all depths, affecting the wave dispersion for all wavelengths, whereas the exponential profile is felt strongly by the short waves with $k \gtrsim \alpha k_{p,0}$ and hardly at all for long waves $k \ll \alpha k_{p,0}$.

Fig. 6a and 6b show the skewness of linear and exponential shear current cases, respectively, calculated according to its definition given by (22b). The theoretical narrow–band predictions in solid blue lines are based on (23b) with the assumption of narrow-band waves in both the absence (i.e. $S = 0$ and $\beta = 0$ in Fig. 6a and 6b, respectively) and presence of a shear current. For both linear shear and exponential shear cases the skewness increases monotonically with S and β, respectively. In the range of shear strengths examined in Fig. 6, the skewness always remains positive. The strongest shear current enhances the skewness by about 86% compared

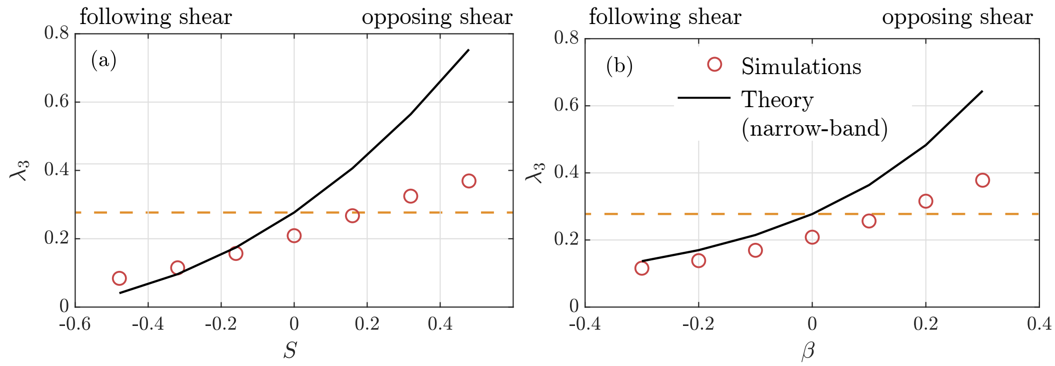

FIG. 6. Skewness of the wave surface elevation for the cases with a linear shear current (a) and exponential shear current (b). The narrow-band theoretical predictions in solid black lines are based on (23b). The dashed line is the no-shear case, for reference.

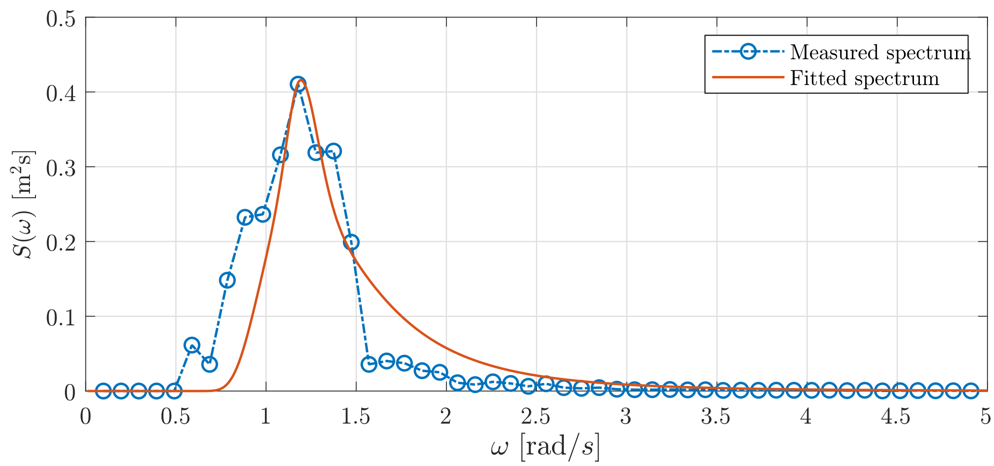

FIG. 7. Power energy spectrum for the Columbia River wave data.

with the cases in the absence of a shear current. The narrow-band assumption for the cases with an exponential shear current always leads to an overestimate of the skewness, compared with the numerical simulations due to the theory in §II applicable to arbitrary bandwidth. In contrast, it may lead to underestimated values for the linear shear and following current cases in the regime where $S \leq -0.2$. The inaccuracy induced by the narrow-band assumption is obvious, which may arise from that the JONSWAP spectrum chosen is not very narrow and that the strong profile shear can lead to a considerable change in the wavelength of all waves prescribed on the JONSWAP spectrum.

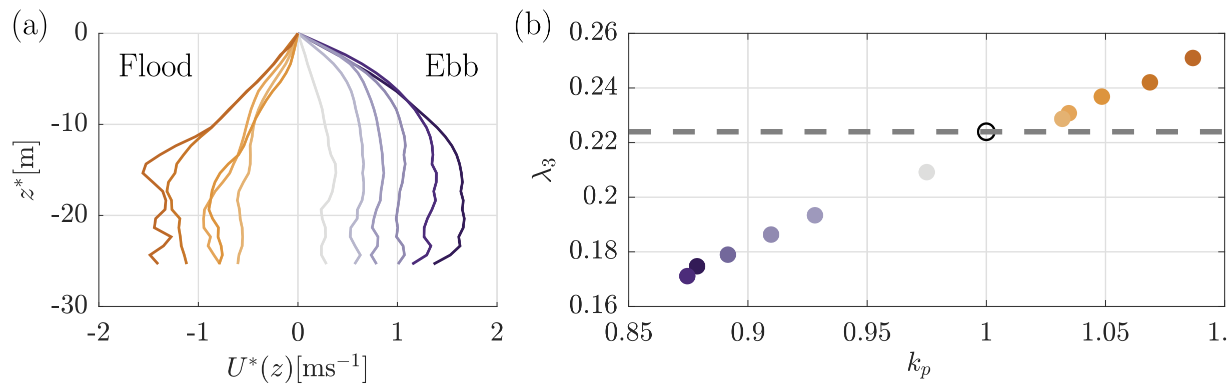

FIG. 8. Skewness of wave surface elevation with Columbia River current and wave spectrum data (a) Considered current profiles, reproduced with kind permission from figure 3 of [54] with the same colour coding, shifted to the surface level and with surface current subtracted. (b) Numerically obtained skewness for the measured wave spectrum of ref. [54] on the currents in panel (a), with corresponding color coding; the ascissa is the shear-shifted peak wave number with $k_p = 1$ corresponding to zero shear (open circle).

E. The Mouth of the Columbia River

As a real–life example we consider the real measured data described in Section IV B 2 to demonstrate and quantify the significant misprediction of wave statistics that would result from neglecting the current's vertical shear. The currents considered, adapted from figure 3 of Zippel & Thomson [54] are shown in Fig. 8a, using the same color coding as in said figure. The surface current was subtracted and the profiles extended to the surface as explained in section IV B 2. As input wave spectrum we fit a JONSWAP spectrum with bandwidth parameter $\nu = 0.6618$ to a representative example among the manywave spectra measured by Zippel and Thomson [54], shown in figure 7. The fit is not excellent, but sufficient to provide a representative example.

Figure 1d shows the weak-shear parameter $\delta(\omega)$ when ω is the given parameter; we argue in appendix E that the appropriate value in this case is $\delta_\omega(\omega) = 2\delta(\omega^2/g)$ where $\delta(k)$ is defined in (35).

1. Skewness

The skewness of simulated results with Columbia River current data are given in Fig. 8b, where k_p is the dimensionless peak wavenumber which depends on the shear current as aforementioned. We chose to use k_p as a representation of the shear strength as it expresses the amount by which the shear changes the wavelength of the wave with peak frequency.

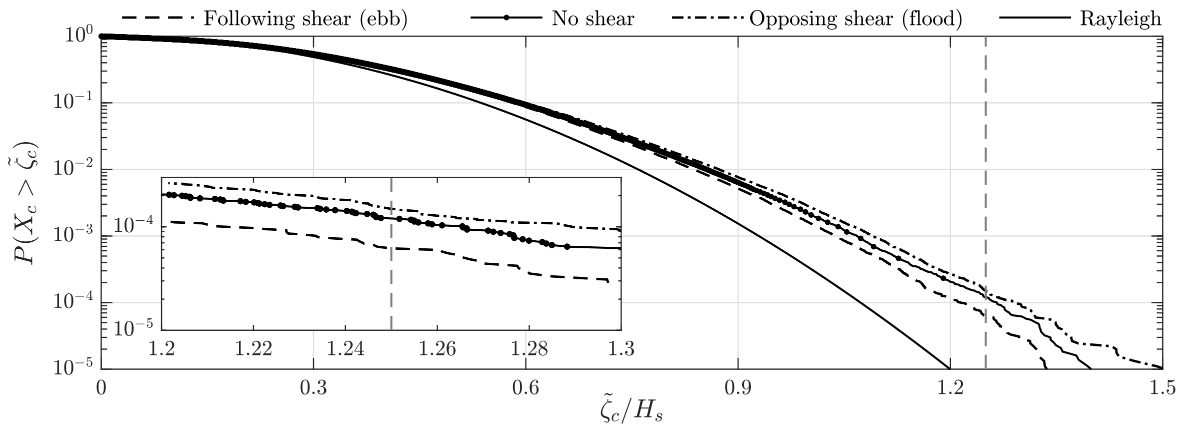

FIG. 9. Exceedance probability of simulated results with the current measured by Zippel & Thomson [54] in the Columbia River (CR) shown in Fig. 1c, equal to the strongest currents in either direction in Fig. 8a. The profiles of the following and opposing CR-current are shown in Figure 1c.

Failure to take into account the presence of shear causes overprediction of skewness by $\approx 24\%$ or underprediction by $\approx 13\%$ during ebb and flood, respectively, as is shown in Fig. 8. Absolute numbers provided by a second-order theory like ours carry significant uncertainty, particularly when the spectrum is not narrow, but show a clear and consistent trend. Held together with Zippel & Thomson's conclusion that wave steepness can be mispridicted by $\pm 20\%$ in these waters in the same conditions if shear is not accounted for [54], there is compelling evidence that shear can be highly significant to the estimation of wave statistics from measured spectra.

2. Rogue wave probability

We also carried out simulations with data from Columbia River (CR) using both the wave spectrum and shear profiles measured in this location by Zippel and Thomson [54]. As usual, rogue wave probability is defined as the probability of crests exceeding $1.25H_s$.

As observed for the model currents in Figure 4, opposing shear enhances the crest heights of large waves while following shear weakens them, leading to increased and decreased exceedance probability, respectively. The rogue wave probability on opposing shear (i.e., a following surface current during ebb) is increased by 36% while on following shear (opposing surface current, during flow) it is decreased by 45%; from 1.12×10^{-4} to 6.20×10^{-5} and 1.52×10^{-4}, respectively. Given that our theory is second order only, these numbers are not quantitatively accurate, but show clearly that shear currents must be accounted for in prediction and modelling of extreme waves.

Note carefully that the rogue wave probability is the probability of *surprisingly* high waves, as discussed by Hjelmervik and Trulsen [30]. Although rogue waves are more than twice as probable on the wave–following flow current than the wave–opposing ebb current, the significant wave height itself is typically much greater in the former case (more than twice as high in the conditions measured in [54], for instance), making for rougher conditions overall. The effect of shear is to reduce the prevalence of very large waves during ebb, a beneficial effect with respect to sealoads and maritime safety.

VI. CONCLUSIONS

In this paper, we develop the second-order (deterministic) theory using perturbation expansion, which is extended from Longuet-Higgins [11] to allow for a depth-dependent background flow whose profile shear can be strong. The new theory can be used to investigate the wave-current interaction and applicable to waves of an arbitrary bandwidth. The linear wave field is solved with the DIM method proposed by Li & Ellingsen [47]. We derived a boundary value problem for the second-order waves, which can be solved numerically. With the additional assumption of narrow-band waves, a second-order accurate statistical model is derived for the skewness, probability density function of surface elevation, and the probability distribution of wave crest, which have accounted for the presence of a depth-dependent background flow.

We carried out numerical simulations for the analysis of wave statistics and examined effects of a shear current. We used a JONSWAP spectrum and several different shear currents as input to generate linear random waves. The second-order waves are solved for numerically based our newly derived theory. The measured wave spectrum and currents from Columbia River by Zippel & Thomson [54] were also used in our simulations.

For linear wave fields the probability distribution of wave surface elevation and wave maxima and average maximum wave crest all satisfy theoretical expressions well as expected. The nonlinear wave fields show similar properties compared with well-known second-order Stokes waves. The wave crests are higher and troughs are flatter than linear wave fields. As a result, the positive tails of the probability density function for wave surface elevation and wave maxima from nonlinear wave fields are longer than linear wave fields while the negative tails of surface elevation are shorter. Also, the largest wave crests in nonlinear wave fields are substantially greater. We found that the opposing shear currents can strengthen such 'nonlinear properties' while the following shear currents can weaken them.

We also found that the additional assumption of narrow-band waves leads to in general negligible and pronounced differences for the following- and opposing-shear case, respectively, when comparing the second-order statistical model with the more general deterministic theory which is applicable to waves with an arbitrary bandwidth.

ACKNOWLEDGMENTS

Z.B. Zheng acknowledges the support from China Scholarship Council through project 201906060137. Y. Li is supported by the Research Council of Norway (RCN) through the FRIPRO mobility project 287389. S.Å. Ellingsen is supported by the European Research Council Consolidator Grant no. 101045299 (*WaTurSheD*), and the RCN grant 325114 (*iMod*). We thank Dr. Seth Zippel and Professor Jim Thomson for the use of the data collected from the Data Assimilation and Remote Sensing for Littoral Applications (DARLA) project and the Rivers and Inlets (RIVET) program (see, e.g., [54] for details). The computer code (MATLAB) used to generate our data is included as supplementary material. We thank the anonymous referees for their valuable suggestions and comments which have improved the quality of the paper.

Appendix A: Flow diagram of numerical implementations

A flow diagram of the numerical implementation used to generate statistics is shown in Figure 10.

Appendix B: The forcing terms of the Rayleigh equation

With the linear wave fields given by (11a,b,c), the nonlinear forcing terms in (14c) are expressed as

$$\hat{\mathcal{N}}_{\pm}^{(2)} =[\mathbf{k}_{\pm}\cdot\partial_z\mathbf{N}_{h,\pm}+k_{\pm}^2 N_{Rz,+}]\cos\psi_{\pm}, \tag{B1a}$$

$$\hat{\mathcal{F}}_{\pm}^{(2)} =[k_{\pm}^2 N_{F1,\pm}-N_{F2,\pm}+N_{F3,\pm+}-N_{F4,\pm}-(\mathbf{U}\cdot\mathbf{k}_{\pm}-\omega_{\pm})\mathbf{k}_{\pm}\cdot N_{h,+}]\sin\psi_{\pm}, \tag{B1b}$$

with $\psi_{\pm}=\psi_1\pm\psi_2$, $\mathbf{N}_{h,i}=[N_{Rx,i},N_{Ry,i}]$,

$$\begin{bmatrix} N_{Rx,\pm} \\ N_{Ry,\pm} \\ N_{Rz,\pm} \end{bmatrix} = \frac{1}{2}\begin{bmatrix} -(k_{1x}\hat{u}_1^{(1)}\hat{u}_2^{(1)} \pm k_{2x}\hat{u}_2^{(1)}\hat{u}_1^{(1)} + k_{1y}\hat{u}_1^{(1)}\hat{v}_2^{(1)} \pm k_{2y}\hat{u}_2^{(1)}\hat{v}_1^{(1)} \mp \hat{u}_1^{(1)\prime}\hat{w}_2^{(1)} - \hat{u}_2^{(1)\prime}\hat{w}_1^{(1)}) \\ -(k_{1x}\hat{v}_1^{(1)}\hat{u}_2^{(1)} \pm k_{2x}\hat{v}_2^{(1)}\hat{u}_1^{(1)} + k_{1y}\hat{v}_1^{(1)}\hat{v}_2^{(1)} \pm k_{2y}\hat{v}_2^{(1)}\hat{v}_1^{(1)} \mp \hat{v}_1^{(1)\prime}\hat{w}_2^{(1)} - \hat{v}_2^{(1)\prime}\hat{w}_1^{(1)}) \\ k_{x1}\hat{w}_1^{(1)}\hat{u}_2^{(1)} + k_{x2}\hat{w}_2^{(1)}\hat{u}_1^{(1)} + k_{y1}\hat{w}_1^{(1)}\hat{v}_2^{(1)} + k_{y2}\hat{w}_2^{(1)}\hat{v}_1^{(1)} \mp \hat{w}_1^{(1)\prime}\hat{w}_2^{(1)} \mp \hat{w}_1^{(1)}\hat{w}_2^{(1)\prime} \end{bmatrix} \tag{B2a}$$

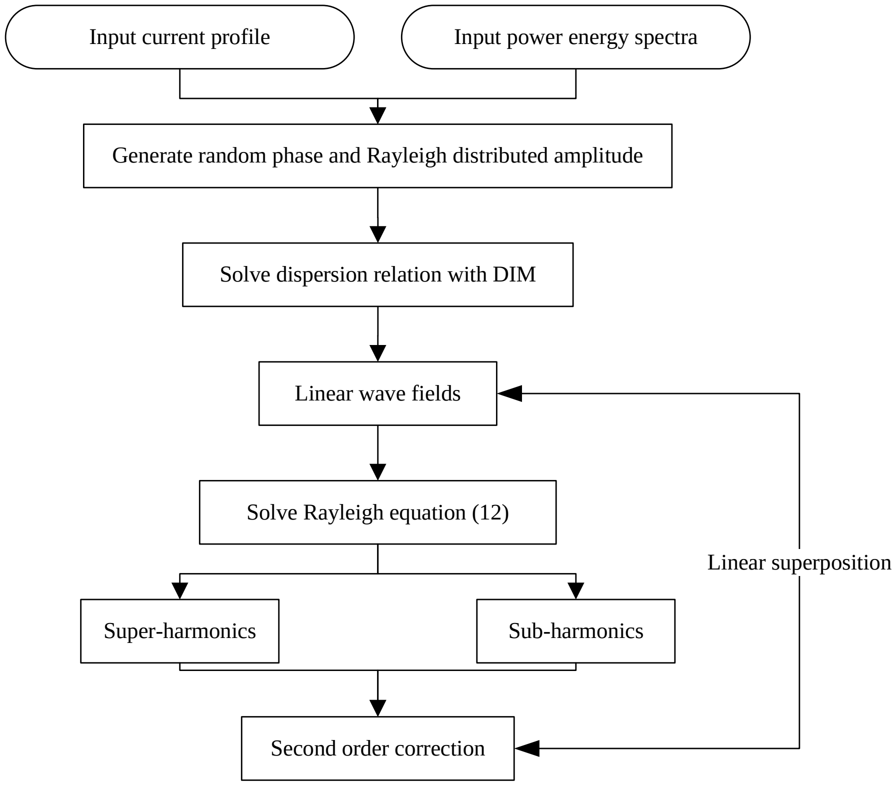

FIG. 10. Numerical procedures of the simulation.

and

$$N_{F1\pm} = -\frac{1}{2}(k_{1x}\hat{u}_2^{(1)}\hat{\zeta}_1^{(1)} + k_{1y}\hat{v}_2^{(1)}\hat{\zeta}_1^{(1)} \pm k_{2x}\hat{u}_1^{(1)}\hat{\zeta}_2^{(1)} \pm k_{2y}\hat{v}_1^{(1)}\hat{\zeta}_2^{(1)}) \tag{B3a}$$

$$N_{F2\pm} = \frac{1}{2}(\mathbf{k}_1^2(\mathbf{k}_1 \cdot \mathbf{U} - \omega_1)\hat{\zeta}_2^{(1)}\hat{P}_1^{(1)\prime} \pm \mathbf{k}_2^2(\mathbf{k}_2 \cdot \mathbf{U} - \omega_2)\hat{\zeta}_1^{(1)}\hat{P}_2^{(1)\prime}) \tag{B3b}$$

$$N_{F3\pm} = -\frac{1}{2}(\mathbf{k}_1^2\hat{\zeta}_2^{(1)}\hat{w}_1^{(1)\prime} \pm \mathbf{k}_2^2\hat{\zeta}_1^{(1)}\hat{w}_2^{(1)\prime}) \tag{B3c}$$

$$N_{F4\pm} = \frac{1}{2}(\mathbf{k}_1^2\mathbf{k}_1 \cdot \mathbf{U}'\hat{P}_1^{(1)}\hat{\zeta}_2^{(1)} \pm \mathbf{k}_2^2\mathbf{k}_2 \cdot \mathbf{U}'\hat{P}_2^{(1)}\hat{\zeta}_1^{(1)}) \tag{B3d}$$

where $\mathbf{k}_1 = [k_{1x}, k_{1y}]$ and $\mathbf{k}_2 = [k_{2x}, k_{2y}]$

Appendix C: Analytical solution for linearly sheared current

We assume the shear profile is given by $\mathbf{U} = (S_0 z, 0)$. The linear solution can be easily solved, which is expressed as [32, 38]

$$\hat{w}^{(1)}(\mathbf{k}, z) = \hat{w}_0^{(1)}(\mathbf{k})\mathrm{e}^{kz} \tag{C1a}$$

$$\hat{\mathbf{u}}^{(1)}(\mathbf{k}, z) = \mathrm{i}\frac{k^2\mathbf{U}' + [(\mathbf{U}\cdot\mathbf{k} - \omega)k - k_x S_0]\mathbf{k}}{(\mathbf{U}\cdot\mathbf{k} - \omega)k^2}\hat{w}_0^{(1)}\mathrm{e}^{kz} \tag{C1b}$$

$$\hat{P}^{(1)}(\mathbf{k}, z) = -\mathrm{i}\frac{(\mathbf{U}\cdot\mathbf{k} - \omega)k - k_x S_0}{k^2}\hat{w}_0^{(1)}\mathrm{e}^{kz} \tag{C1c}$$

$$\hat{w}_0^{(1)}(\mathbf{k}) = -\mathrm{i}\hat{\zeta}^{(1)}(\mathbf{k})\omega \tag{C1d}$$

where $\mathbf{k} = (k_x, k_y)$, $k = \sqrt{k_x^2 + k_y^2}$ and the subscript '0' denotes the evaluation at a undisturbed surface $z = 0$. The dispersion relation for linear waves in a linearly sheared current is given by [32, 38]

$$\omega = -\frac{S_0 k_x}{2k} \pm \sqrt{k + \frac{S_0^2 k_x^2}{4k^2}}, \tag{C2}$$

where '+' and '−' denotes the waves propagating 'downstream' and 'upstream' relative to the current, respectively.

Substituting the linear solution into the forcing terms of second-order equations (17), we obtain an inhomogeneous boundary value problem for the second-order vertical velocity $w^{(2)}$. The general solution to this boundary value problem in the Fourier space should admit the form

$$\hat{w}_{\pm}^{(2)}(\mathbf{k}_1, \mathbf{k}_2, z) = B_{1\pm}(\mathbf{k}_1, \mathbf{k}_2)\mathrm{e}^{k_\pm z} + \hat{w}_{cross}(\mathbf{k}_1, \mathbf{k}_2, z), \tag{C3}$$

where the deepwater boundary condition was used, the first term on the right hand side of the equation is due to the forcing at a still water surface and the homogeneous Rayleigh equation, and $\hat{w}_{cross}$is a particular solution of the inhomogeneous Rayleigh equation given by [38]

$$\hat{w}_{cross}(\mathbf{k}_1, \mathbf{k}_2, z) = -\frac{i}{2k_\pm}\frac{\hat{w}_{0,1}^{(1)}\hat{w}_{0,2}^{(1)}}{k_{\pm x}S_0}\frac{k_{1x}k_{2y} - k_{1y}k_{2x}}{k_1 k_2}\mathrm{e}^{(k_1+k_2)z}\sum_{i,j=1}^{3}\Bigg[\frac{\pm b_{ij}}{(\xi_i - z)^{j-1}}$$

$$\times \tilde{E}_j[k_\pm(\xi_i - z)]\Bigg], \tag{C4}$$

with $\hat{w}_{0,j}^{(1)} = \hat{w}_0^{(1)}(\mathbf{k}_j)$ for $j = 1$ and $j = 2$,

$$b_{ij} = \sum_{m=j}^{3}\frac{-a_{im}}{(\xi_i - \xi_3)^{m-j+1}}, \quad i = 1, 2;\ b_{31} = -b_{11} - b_{21};\ b_{32} = b_{33} = 0, \tag{C5a}$$

$$\xi_1 = \frac{\omega_1}{k_{1x}S_0}, \quad \xi_2 = \frac{\omega_2}{k_{2x}S_0}, \quad \xi_3 = \frac{\omega_\pm}{k_x S_0}, \tag{C5b}$$

$$\tilde{E}_j(\mu) = \mathrm{e}^{\mu}\mu^{j-1}\int_{\mu}^{\infty}\frac{\mathrm{e}^{-\tau}}{\tau^j}\mathrm{d}\tau. \tag{C5c}$$

Assuming $\xi_1 \neq \xi_2$, the coefficients in (C5) are expressed as

$$a_{i1} =(-1)^i \left[k_1 k_2 - \mathbf{k}_1 \cdot \mathbf{k}_2 - \frac{k_1 + k_2}{\xi_1 - \xi_2} \frac{k_{1x} k_{2y} - k_{1y} k_{2x}}{k_1 k_2} \tan\theta_m\right] \tan\theta_i \tag{C6a}$$

$$a_{i2} =(-1)^i \frac{1}{k_i} \left[k_1 k_2 - \mathbf{k}_1 \cdot \mathbf{k}_2 - \frac{k_i}{\xi_1 - \xi_2} \frac{k_{1x} k_{2y} - k_{1y} k_{2x}}{k_1 k_2} \tan\theta_m\right] \tan\theta_i \tag{C6b}$$

$$a_{i3} =(-1)^i \frac{k_m}{k_i} \tan\theta_i, \tag{C6c}$$

where $i, m \in \{1, 2\}$ so that $i \neq m$ and $\tan\theta_i = k_{iy}/k_{ix}$. The undetermined coefficients $B_{1\pm}$ is solved by inserting (C3) into the combined boundary condition (17b). Then, the surface elevation is obtained from (19).

Appendix D: Effects of current continuation on skewness

We here compare three alternative, physically reasonable ways in which profiles measured using ADCP can be extended from the shallowest measurement point — $z = -1.35\,\mathrm{m}$ for the Columbia River measurements we use [64] — up to the surface. These are: extrapolation using a polynomial fit, shifting the profile upwards so that the shallowest measurement point is set to surface level (used, *inter alia*, in refs. [82, 96]), and the highly conservative approach of continuing the current profile to the surface with zero shear. These are referred as extended profile, shifted profile and zero surface shear profile, respectively and are shown in figure 11a.

We compare wave skewness in these three case, the results are given in Fig. 11. Again, the k_p in Fig.11b is the dimensionless peak wavenumber as in Fig. 8, where $k_p = 1$ corresponds to the case without shear current whereas the modifications to the dispersion relation due to shear shifts the value. Values $k_p > 1$ correspond to adverse shear and *vice versa*. A plot of the calculated skewness for the different cases shows that the difference in skewness is hardly discernable.

Appendix E: Dimensionless weak–shear parameter for given ω

Let the depth-averaged shear be small, of order a small parameter $\delta \ll 1$. Assuming the wave number k given, Stewart and Joy [55] derived the approximate dispersion relation $\omega(k)$ which may be written [60]

$$\omega^*(k^*) \approx \sqrt{gk^*}[1 - \delta(k^*)] + \mathcal{O}(\delta^2), \tag{E1}$$

with the small-shear parameter $\delta(k^*)$ defined in (35). It was shown [60] that a sufficient criterion for the Stewart & Joy approximation to be good is that $\delta_\omega \ll 1$.

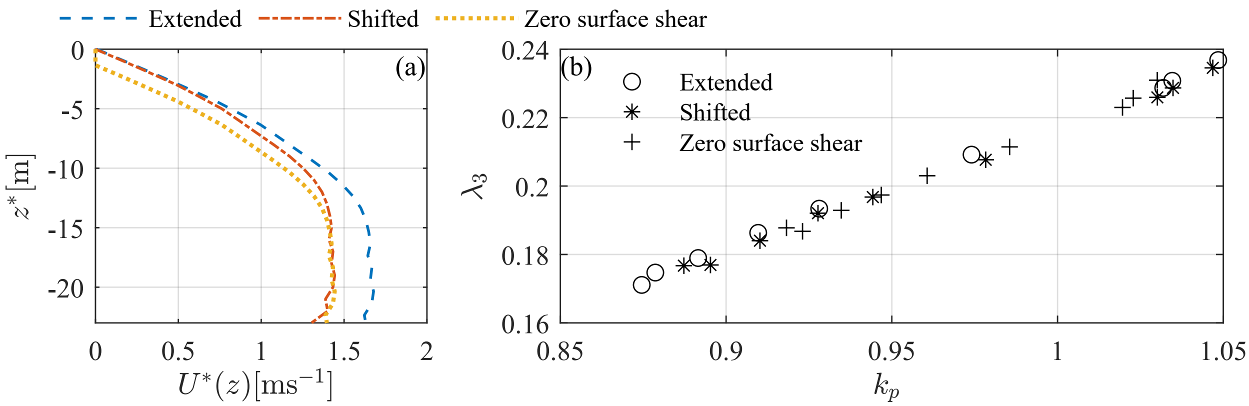

FIG. 11. Skewness of wave surface elevation for different profiles. (a) Comparison of shear profiles with three approaches. (b) Numerically obtained skewness, 'o': extended profiles, '*': shifted profiles, '+': zero surface shear profiles. Case chosen is same with Fig. 8 except that two strongest opposing shears are excluded here.

Conversely (i.e., for given ω^*) the presence of shear modifies k slightly, and we write

$$k^* = k_0^*[1 + \delta_\omega(\omega^*)] + \mathcal{O}(\delta_\omega^2) \tag{E2}$$

with $k_0^* = (\omega^*)^2/g$, and clearly $\delta_\omega \sim \delta$. We seek to find δ_ω. Inserting (E2) into (E1) via (35) and noting that $\sqrt{gk_0^*} = \omega^*$,

$$\begin{aligned}\omega^* =&\omega^*\sqrt{1+\delta_\omega}[1 - \delta(k_0^*)] + \mathcal{O}(\delta^2)\\ =&\omega^*[1 + \tfrac{1}{2}\delta_\omega - \delta(k_0^*)] + \mathcal{O}(\delta^2).\end{aligned} \tag{E3}$$

Internal consistency thus demands

$$\delta_\omega(\omega^*) = 2\delta(k_0^*). \tag{E4}$$

---

[1] C. Kharif, E. Pelinovsky, and A. Slunyaev, *Rogue waves in the ocean* (Springer Science & Business Media, 2008).

[2] L. Cavaleri, S. Abdalla, A. Benetazzo, L. Bertotti, J. R. Bidlot, Breivik, S. Carniel, R. E. Jensen, J. Portilla-Yandun, W. E. Rogers, A. Roland, A. Sanchez-Arcilla, J. M. Smith, J. Staneva, Y. Toledo, G. P. van Vledder, and A. J. van der Westhuysen, Wave modelling in coastal and inner seas, Prog. Oceanogr. **167**, 164 (2018).

[3] J. M. Dudley, G. Genty, A. Mussot, A. Chabchoub, and F. Dias, Rogue waves and analogies in optics and oceanography, Nat. Rev. Phys **1**, 675 (2019).

[4] T. B. Benjamin and J. E. Feir, The disintegration of wave trains on deep water Part 1. theory, J. Fluid Mech. **27**, 417 (1967).

[5] P. A. E. M. Janssen, Nonlinear four-wave interactions and freak waves, J. Phys. Oceanogr. **33**, 863 (2003).

[6] B. White and B. Fornberg, On the chance of freak waves at sea, J. Fluid Mech. **335**, 113 (1998).

[7] T. Janssen and T. Herbers, Nonlinear wave statistics in a focal zone, J. Phys. Oceanogr. **39**, 1948 (2009).

[8] J. Gao, X. Ma, G. Dong, H. Chen, Q. Liu, and J. Zang, Investigation on the effects of Bragg reflection on harbor oscillations, Coast. Eng. **170**, 103977 (2021).

[9] K. Trulsen, A. Raustøl, S. Jorde, and L. Rye, Extreme wave statistics of long-crested irregular waves over a shoal, J. Fluid Mech. **882** (2020).

[10] Y. Li, S. Draycott, Y. Zheng, Z. Lin, T. Adcock, and T. van den Bremer, Why rogue waves occur atop abrupt depth transitions, J. Fluid Mech. **919** (2021).

[11] M. S. Longuet-Higgins, Resonant interactions between two trains of gravity waves, J. Fluid Mech. **12**, 321 (1962).

[12] M. S. Longuet-Higgins, The effect of non-linearities on statistical distributions in the theory of sea waves, J. Fluid Mech. **17**, 459 (1963).

[13] M. A. Tayfun, Narrow-band nonlinear sea waves, J. Geophys. Res. **85**, 1548 (1980).

[14] M. A. Tayfun, Effects of spectrum band width on the distribution of wave heights and periods, Ocean Eng. **10**, 107 (1983).

[15] M. A. Tayfun, On narrowband representation of ocean waves: 1. theory, J. Geophys. Res.: Oceans **91**, 7743 (1986).

[16] J. Dalzell, A note on finite depth second-order wavewave interactions, Appl. Ocean Res. **21**, 105 (1999).

[17] G. Z. Forristall, Wave crest distributions: Observations and second-order theory, J. Phys. Oceanogr. **30**, 1931 (2000).

[18] F. Arena and F. Fedele, A family of narrow-band non-linear stochastic processes for the mechanics of sea waves, Eur. J. Mech. B Fluids **21**, 125 (2002).

[19] A. A. Toffoli, M. Onorato, A. V. Babanin, E. Bitner-Gregersen, A. R. Osborne, and J. Monbaliu, Second-order theory and setup in surface gravity waves: A comparison with experimental data, J. Phys. Oceanogr. **37**, 2726 (2007).

[20] A. Toffoli, M. Onorato, E. Bitner-Gregersen, A. R. Osborne, and A. V. Babanin, Surface gravity waves from direct numerical simulations of the Euler equations: A comparison with second-order theory, Ocean Eng. **35**, 367 (2008).

[21] M. S. Longuet-Higgins, On the statistical distribution of the height of sea waves, J. Marine Res. **11**, 245 (1952).

[22] P. Petrova, Z. Cherneva, and C. G. Soares, Distribution of crest heights in sea states with abnormal waves, Appl. Ocean Res. **28**, 235 (2006).

[23] F. Fedele and M. A. Tayfun, On nonlinear wave groups and crest statistics, J. Fluid Mech. **620**, 221 (2009).

[24] F. Fedele, J. Herterich, A. Tayfun, and F. Dias, Large nearshore storm waves off the Irish coast, Sci. Rep. **9**, 15406 (2019).

[25] V. I. Shrira and A. V. Slunyaev, Trapped waves on jet currents: asymptotic modal approach, J. Fluid Mech. **738**, 65 (2014).

[26] V. I. Shrira and A. V. Slunyaev, Nonlinear dynamics of trapped waves on jet currents and rogue waves, Phys. Rev. E **89**, 041002(R) (2014).

[27] D. H. Peregrine, Interaction of water waves and currents, Adv. Appl. Mech. **16**, 9 (1976).

[28] J. R. Stocker and D. H. Peregrine, The current-modified nonlinear Schrödinger equation, J. Fluid Mech. **399**, 335 (1999).

[29] C. W. Curtis, J. D. Carter, and H. Kalisch, Particle paths in nonlinear Schrödinger models in the presence of linear shear currents, J. Fluid Mech. **855**, 322 (2018).

[30] K. B. Hjelmervik and K. Trulsen, Freak wave statistics on collinear currents, J. Fluid Mech. **637**, 267 (2009).

[31] M. Onorato, D. Proment, and A. Toffoli, Triggering rogue waves in opposing currents, Phys. Rev. Lett. **107**, 184502 (2011).

[32] S. Å. Ellingsen, Oblique waves on a vertically sheared current are rotational, Eur. J. Mech. B. Fluids **56**, 156 (2016).

[33] R. A. Dalrymple, A finite amplitude wave on a linear shear current, J. Geophys. Res. **79**, 4498 (1974).

[34] R. Thomas, C. Kharif, and M. Manna, A nonlinear Schrödinger equation for water waves on finite depth with constant vorticity, Phys. Fluids **24**, 127102 (2012).

[35] J. Touboul and C. Kharif, Effect of vorticity on the generation of rogue waves due to dispersive focusing, Nat. Hazards **84**, 585 (2016).

[36] B. Liao, G. Dong, Y. Ma, and J. L. Gao, Linear-shear-current modified Schrödinger equation for gravity waves in finite water depth, Phys. Rev. E **96**, 043111 (2017).

[37] H. C. Hsu, C. Kharif, M. Abid, and Y. Y. Chen, A nonlinear Schrödinger equation for gravity–capillary water waves on arbitrary depth with constant vorticity. part 1, J. Fluid Mech. **854**, 146 (2018).

[38] A. H. Akselsen and S. Ellingsen, Weakly nonlinear transient waves on a shear current: Ring waves and skewed langmuir rolls, J. Fluid Mech. **863**, 114 (2019).

[39] A. I. Baumstein, Modulation of gravity waves with shear in water, Stud. Appl. Math. **100**, 365 (1998).

[40] J. N. Steer, A. G. Borthwick, D. Stagonas, E. Buldakov, and T. S. van den Bremer, Experimental study of dispersion and modulational instability of surface gravity waves on constant vorticity currents, J. Fluid Mech. **884** (2020).

[41] N. Pizzo, L. Lenain, O. Rømcke, S. Å. Ellingsen, and B. K. Smeltzer, The role of Lagrangian drift in the geometry, kinematics and dynamics of surface waves, J. Fluid Mech. (accepted) (2023).

[42] M. Francius and C. Kharif, Two-dimensional stability of finite-amplitude gravity waves on water of

finite depth with constant vorticity, J. Fluid Mech. **830**, 631 (2017).

[43] A. Abrashkin and E. Pelinovsky, Lagrange form of the nonlinear Schrödinger equation for low-vorticity waves in deep water, Nonlinear Process Geophys. **24**, 255 (2017).

[44] A. G. Voronovich, Propagation of internal and surface gravity waves in the approximation of geometrical optics, Izv. - Atmos. Ocean. Phys. **12**, 850 (1976).

[45] B. Quinn, Y. Toledo, and V. Shrira, Explicit wave action conservation for water waves on vertically sheared flows, Ocean Model. **112**, 33 (2017).

[46] S. Banihashemi, J. T. Kirby, and Z. Dong, Approximation of wave action flux velocity in strongly sheared mean flows, Ocean Model. **116**, 33 (2017).

[47] Y. Li and S. Ellingsen, A framework for modeling linear surface waves on shear currents in slowly varying waters, J. Geophys. Res.: Oceans **124**, 2527 (2019).

[48] S. Banihashemi and J. T. Kirby, Approximation of wave action conservation in vertically sheared mean flows, Ocean Model. **143**, 101460 (2019).

[49] I. Cummins and C. Swan, Vorticity effects in combined waves and currents, Coast. Eng. Proc. **1** (1994).

[50] T. Waseda, T. Kinoshita, L. Cavaleri, and A. Toffoli, Third-order resonant wave interactions under the influence of background current fields, J. Fluid Mech. **784**, 51 (2015).

[51] B. K. Smeltzer, E. sy, and S. A. Ellingsen, Observation of surface wave patterns modified by sub-surface shear currents, J. Fluid Mech. **873**, 508 (2019).

[52] F. Ardhuin, Small-scale open ocean currents have large effects on wind wave heights, J. Geophys. Res.: Oceans **122**, 1 (2017).

[53] F. Ardhuin, L. Mari, N. Rascle, P. Forget, and A. Roland, Observation and estimation of Lagrangian, Stokes, and Eulerian currents induced by wind and waves at the sea surface, J. Phys. Oceanogr. **39**, 2820 (2009).

[54] S. Zippel and J. Thomson, Surface wave breaking over sheared currents: Observations from the mouth of the Columbia River, J. Geophys. Res.: Oceans **122**, 3311 (2017).

[55] R. H. Stewart and J. W. Joy, HF radio measurements of surface currents, Deep-Sea Res. Oceanogr. Abstracts **21**, 1039 (1974).

[56] R. A. Skop, Approximate dispersion relation for wave-current interactions, J. Waterw. Port, Coast. Ocean Eng. **113**, 187 (1987).

[57] J. T. Kirby and T. Chen, Surface waves on vertically sheared flows: approximate dispersion relations, J. Geophys. Res. Oceans **94**, 1013 (1989).

[58] V. Zakharov and V. Shrira, About the formation of angular spectrum of wind waves, Zh. Eksp. Teor. Fiz **98**, 1941 (1990).

[59] V. I. Shrira, Surface waves on shear currents: solution of the boundary-value problem, J. Fluid Mech. **252**, 565 (1993).

[60] S. Å. Ellingsen and Y. Li, Approximate dispersion relations for waves on arbitrary shear flows, J. Geophys. Res.: Oceans **122**, 9889 (2017).

[61] N. J. Laxague, B. K. Haus, D. G. Ortiz-Suslow, C. J. Smith, G. Novelli, H. Dai, T. Özgökmen, and H. C. Graber, Passive optical sensing of the near-surface wind-driven current profile, J. Atmos. Ocean. Technol. **34**, 1097 (2017).

[62] N. J. Laxague, T. M. Özgökmen, B. K. Haus, G. Novelli, A. Shcherbina, P. Sutherland, C. M. Guigand, B. Lund, S. Mehta, M. Alday, *et al.*, Observations of near-surface current shear help describe oceanic oil and plastic transport, Geophys. Res. Lett. **45**, 245 (2018).

[63] J. Wu, Sea-surface drift currents induced by wind and waves, J. Phys. Oceanogr. **13**, 1441 (1983).

[64] L. F. Kilcher and J. D. Nash, Structure and dynamics of the Columbia River tidal plume front, J. Geophys. Res.: Oceans **115** (2010).

[65] M. J. Tucker, P. G. Challenor, and D. J. T. Carter, Numerical simulation of a random sea: a common error and its effect upon wave group statistics, Appl. Ocean Res. **6**, 118 (1984).

[66] K. Hasselmann, On the non-linear energy transfer in a gravity-wave spectrum part 1. general theory, J. Fluid Mech. **12**, 481 (1962).

[67] D. G. Dommermuth and D. K. P. Yue, A high-order spectral method for the study of nonlinear gravity waves, J. Fluid Mech. **184**, 267 (1987).

[68] B. J. West, K. A. Brueckner, R. S. Janda, D. M. Milder, and R. L. Milton, A new numerical method for surface hydrodynamics, J. Geophys. Res.: Oceans **92**, 11803 (1987).

[69] Y. Li and X. Li, Weakly nonlinear broadband and multi-directional surface waves on an arbitrary depth: a framework, stokes drift, and particle trajectories, Phys. Fluids **33** (2021).

[70] M. A. Srokosz and M. S. Longuet-Higgins, On the skewness of sea-surface elevation, J. Fluid Mech. **164**, 487 (1986).

[71] A. D. D. Craik, Resonant gravity-wave interactions in a shear flow, J. Fluid Mech. **34**, 531 (1968).

[72] K. F. Hasselmann, T. P. Barnett, E. Bouws, H. Carlson, D. E. Cartwright, K. Eake, J. Euring, A. Gicnapp, D. Hasselmann, and P. Kruseman, Measurements of wind wave growth and swell decay during the Joint North Sea Wave Project (JONSWAP), Dtsch. Hydrogr. Z. **8**, 95 (1973).

[73] K. Dysthe, H. Socquet-Juglard, K. Trulsen, H. E. Krogstad, and J. Liu, "freak" waves and large-scale simulations of surface gravity waves, in *Proc. 14th Aha Huliko a Hawaiian Winter Workshop* (Citeseer, 2005).

[74] H. Socquet-Juglard, K. Dysthe, K. Trulsen, H. E. Krogstad, and J. Liu, Probability distributions of surface gravity waves during spectral changes, J. Fluid Mech. **542**, 195 (2005).

[75] M. S. Longuet-Higgins, On the joint distribution of the periods and amplitudes of sea waves, J. Geophys. Res. **80**, 2688 (1975).

[76] Z. Dong and J. T. Kirby, Theoretical and numerical study of wave-current interaction in strongly-sheared flows, Coast. Eng. Proc. **1**, 2 (2012).

[77] E. P. Elias, G. Gelfenbaum, and A. J. Van der Westhuysen, Validation of a coupled waveflow model in a highenergy setting: The mouth of the Columbia River, J. Geophys. Res. Oceans **117** (2012).

[78] P. Maxwell, B. K. Smeltzer, and S. Å. Ellingsen, The error in predicted phase velocity of surface waves

atop a shear current with uncertainty, Water Waves , 1 (2019).

[79] J. Campana, E. Terrill, and T. De Paolo, Observations of surface current and current shear using X-band radar, in *Current, Waves and Turbulence Measurement (CWTM), 2015 IEEE/OES Eleventh* (IEEE, 2015) pp. 1–5.

[80] B. Lund, B. K. Haus, J. Horstmann, H. C. Graber, R. Carrasco, N. J. Laxague, G. Novelli, C. M. Guigand, and T. M. Özgökmen, Near-surface current mapping by shipboard marine X-band radar: A validation, J. Atmos. Ocean. Technol. **35**, 1077 (2018).

[81] V. Kudryavtsev, V. Shrira, V. Dulov, and V. Malinovsky, On the vertical structure of wind-driven sea currents, J. Phys. Oceanogr. **38**, 2121 (2008).

[82] Y. Li, B. K. Smeltzer, and S. Å. Ellingsen, Transient wave resistance upon a real shear current, Eur. J. Mech. B/Fluids. **73**, 180 (2019).

[83] Y. Goda, *Random seas and design of maritime structures*, 3rd ed., Vol. 33 (World Scientific Publishing Company, 2010).

[84] P. A. E. M. Janssen, On a random time series analysis valid for arbitrary spectral shape, J. Fluid Mech. **759**, 236 (2014).

[85] F. Barbariol, J.-R. Bidlot, L. Cavaleri, M. Sclavo, J. Thomson, and A. Benetazzo, Maximum wave heights from global model reanalysis, Prog. Oceanogr. **175**, 139 (2019).

[86] D. E. Cartwright and Longuet-Higgins, The statistical distribution of the maxima of a random function, Proc. R. Soc. Lond. **237**, 212 (1956).

[87] S. O. Rice, Mathematical analysis of random noise, Bell Syst. Tech. J. **23**, 282 (1944).

[88] R. E. Haring, A. R. Osborne, and L. P. Spencer, Extreme wave parameters based on continental shelf storm wave records, in *Proceedings of the fifteenth Coastal Engineering Conference* (1976) pp. 151–170.

[89] D. L. Kriebel and T. H. Dawson, Nonlinearity in wave crest statistics, in *Proceedings of the Second International Conference on Wave Measurement and Analysis* (1993) pp. 61–75.

[90] N. E. Huang, L. F. Bliven, S. R. Long, and C.-C. Tung, An analytical model for oceanic whitecap coverage, J. Phys. Oceanogr. **16**, 1597 (1986).

[91] D. Kriebel and T. Dawson, Nonlinear effects on wave groups in random seas, J. Offshore Mech. Arct. Eng. (1991).

[92] M. Prevosto, H. Krogstad, and A. Robin, Probability distributions for maximum wave and crest heights, Coast. Eng. **40**, 329 (2000).

[93] K. Dysthe, H. E. Krogstad, and P. Muller, Oceanic rogue waves, Annu. Rev. Fluid Mech. **40**, 287 (2008).

[94] M. S. Longuet-Higgins, On the statistical distribution of the heights of sea waves, J. Mar. Res. **11**, 245 (1952).

[95] H. E. Krogstad, J. Liu, H. Socquet-Juglard, K. B. Dysthe, and K. Trulsen, Spatial extreme value analysis of nonlinear simulations of random surface waves, in *International Conference on Offshore Mechanics and Arctic Engineering*, Vol. 37440 (2004) pp. 285–295.

[96] B. K. Smeltzer and S. Å. Ellingsen, Surface waves on currents with arbitrary vertical shear, Phys. Fluids **29**, 047102 (2017).